DESIGN, FABRICATION AND ASSEMBLY OF 3-D MICROSTRUCTURES

by

Ping Zhang

Presented to the Faculty of the Graduate School of

The University of Texas at Arlington in Partial Fulfillment

of the Requirements

for the Degree of

DOCTOR OF PHILOSOPHY

THE UNIVERSITY OF TEXAS AT ARLINGTON

May 2007

Copyright © by Ping Zhang 2007

All Rights Reserved

ACKNOWLEDGEMENTS

I would like to express my sincere gratitude to my adviser, Professor Jung-Chin Chiao, for all of his support, guidance, and encouragements throughout my graduate study at UTA. It was because of him and his ideas which lead me to MEMS and thus opening the doors to MEMS for me. I would also like to thank Dr. Wooho Lee for his valuable opinion and help with direct assembly. I also want to thank Professor Weidong Zhou, Professor Donald Butler, and Professor Enjun Xiao for their kind help and precious time in serving on my graduate committee. Finally, I would also like to thank all the students in my group, the faculty, staff and lab members at Automation and Robotic Research Institute, UTA Nanofab, and Stanford Nanofabrication Facility, for their advice, technical expertise, and assistance.

This dissertation is dedicated to my parents and my sister for their endless love and support. I'm especially grateful to my dear friends for their support all the time.

April 10, 2007

.

ABSTRACT

DESIGN, FABRICATION AND ASSEMBLY OF 3-D MCIRO STRUCTURES

Publication No. ______

PING ZHANG, PhD.

The University of Texas at Arlington, 2007

Supervising Professor: Jung-Chih Chiao

The primary goal of a micro-electro-mechanical system (MEMS) is to integrate electronics, sensors and actuators into a tiny system, which can be easily fabricated and packaged. Currently there is no standard process for manufacturing all the sub-components since a lot of them are made from different materials and fabrication technologies. Therefore, there is a great interest to develop a reliable manufacturing approach that allows for the integration of multiple micro devices on a single chip.

This work describes two approaches to achieve this heterogeneous integration: (1) hybrid material integration by introducing new materials into a well-known self-assembly platform (PolyMUMPs) to develop new devices which cannot be achieved by a conventional process. Organic polymer was applied on self-assembled polysilicon microstructures to create new optomechanical devices which can work together with

existing micro devices on the same platform. (2) Direct integration of different microcomponents on a common platform by using direct micoassembly. A new active joining mechanism was proposed for this purpose. It can be used for the assembly of microcomponents that are made of different materials, dimensions and shapes.

Both of the two techniques have been successfully demonstrated in this thesis. The microparts have been designed, fabricated, and then assembled into self-aligned 3-D out-of-plane structures. In the first approach, polymer was successfully integrated as the optical interface of a transmission-type thin-film filter with self-assembled microstructures. It overcame the inherent high absorption of optical signals in polysilicon, which has restricted its application only to reflection-type devices. In the second approach, an innovative active lock mechanism is developed. It provides both the mechanical and electrical interconnections between the microparts and the target substrate or subassembly. This technique allows each of the microcomponents to be fabricated optimally using respective processes then assembled together. Several proof-of-concept devices, such as free space filters and multiple micro-manipulators for parallel assembly, have been constructed.

The results of this work have provided a new way for heterogeneous integration of 3-D microstructures and have resulted in a number of contributions to the MEMS field.

TABLE OF CONTENTS

ACKNOWLEDGEMENTS iii

ABSTRACT iv

LIST OF ILLUSTRATIONS x

LIST OF TABLES xiv

Chapter

1. INTRODUCTION 1

1.1 Motivation 1

1.2 Research Objective 2

1.3 Background: Assembly Technologies and Interconnection 2

1.3.1. Bonding 2

1.3.2. Self-Assembly 4

1.3.2.1. Binding Sites 4

1.3.2.2. Hinged Structure 5

1.3.3. Direct Assembly 6

1.3.4. Interconnection 7

1.4 Thesis Overview 8

1.5 Thesis Contributions 9

2. HYBRID MATERIAL INTEGRATION BY SELF-ASSEMBLY 12

2.1 Methodology 12

2.2 Introduction of PolyMUMPs 13

2.3 Microcomponent Design 14

2.3.1. Scratch Drive Actuator 14

2.3.2. 3-D Hinge 15

2.4 Filter Design 16

2.4.1. Mechanical Design 16

2.4.2. Optical Design 18

2.5 Fabrication 21

2.5.1. Challenges 21

2.5.2. Choosing Polymer 22

2.5.3. Fabrication process 23

2.6 Results 24

2.6.1. Fabrication Result 24

2.6.2. Material Property and Characterization 26

2.6.3. Assembly Result 27

2.6.4. Optical Measurement 28

2.6.5. Summary 31

3. INTEGRATION OF MICROCOMPONENTS BY DIRECT ASSEMBLY 32

3.1 The Overview of Assembly Requirement 32

3.2 Microassembly System 33

3.3 Overview of Assembly Process 35

4. ACTIVE JOINING MECHANISM 37

4.1 Methodology 37

4.1.1. Choosing Actuators 38

4.1.2. Overview of Assembly 39

4.2 Design Architecture 39

4.2.1. Active Lock Concept 39

4.2.1.1. Single Chevron Model (SCM) 41

4.2.1.2. Double Chevron Model (DCM) 41

4.2.2. Actuator Design 42

4.2.2.1. Deflection 42

4.2.2.2. Force 44

4.2.3. Micropart Design 46

4.3 Fabrication Processes 47

4.4 Assembly Procedures 50

4.5 Characterization 53

4.5.1. Before Assembly: Socket Opening 53

4.5.2. After Assembly: Force Characterization 54

4.5.2.3. Experimental Setup 54

4.5.2.4. Measured Results 56

4.6 Soldering 59

4.6.1. Process Requirements 59

4.6.2. Experiments and Primary Results 61

4.6.3. Summary 63

5. APPLICATIONS 64

5.1 DWDM 64

5.1.1. Socket Design and Assembly 64

5.1.2. Experimental Demonstration 67

5.1.3. Results 68

5.1.3.1. Direct Measurement of Filter Chips 68

5.1.3.2. Measured Results of the Assembled Chips 69

5.2 Active Parallel Assembly 72

5.3 Future Work 75

6. CONCLUSION 80

REFERENCES 82

BIOGRAPHICAL INFORMATION 91

LIST OF ILLUSTRATIONS

Figure Page

2.1 (a) A SEM photo, (b) a schematic drawing and
(c) a step motion model of the scratch drive actuator....................................... 15

2.2 (a) 3-D model of the fixed hinge. (b) The cross-sectional
view along the line A--B... 16

2.3 (a) 3-D model of the movable hinge. (b) The cross-sectional
view along the line A--B... 16

2.4 Device architecture of the micro filter. (a) The SDA is connected
to the hinged polysilicon frame without polymer coating.
(b) Polymer film acts as the optical interface supported by the
polysilicon frame. (c) The step motion of scratch drive actuators
lifts the frame up. (d) The frame pivots out of plane and stands
perpendicularly to the substrate after assembly with an incident
laser shone normal to the filter surface.. 17

2.5 Physical layout of the assembly structures. 18

2.6 (a) A Fabry-Perot etalon. (b) The transmittance spectral shape. 19

2.7 Simulation results of the Fabry-Perot etalon with polymer and Si
cavities. The cavity thicknesses are (a) 3 μm and (b) 10 μm, respectively. 20

2.8 The microscope pictures of PirlIII patterns (a) before and (b) after release...... 22

2.9 Cross-sectional views of the micro filter in post fabrication processes............ 24

2.10 Microscope photos when process the filter device during
post fabrication. (a) The MEMS chip without applying polymer.
(b) After coating polymer on the polysilicon support frame.
(c) After the curing procedure. (d) After releasing the chip in BOE. 25

2.11 SEM photo of the polysilicon support frame coated with the polymer film. .. 26

2.12 The plot of the measured absorption coefficient of PI2737. 26

2.13 The plot of the thickness of the cured
polymer film as a function of spin speed... 27

2.14 The plot of the measured surface profile of the cured-polymer filter............. 27

2.15 An SEM photo of the polymer filter
supported by the MEMS frame and actuators. 28

2.16 A photo of the experimental setup... 28

2.17 The configuration of the optical measurement. 29

2.18 The plot of theory and experiment data of transmission spectrum................. 30

3.1 A schematic drawing of the 3-D micro assembly system................................ 34

3.2 A photo of the system setup.. 34

3.3 A photo of using a vacuum gripper to manipulate microparts. 36

4.1 The design concept of active joining mechanism is
illustrated by (a) single chevron model and
(b) double chevron model respectively.. 40

4.2 The (a) top view and (b) 3-D view of the single chevron model...................... 41

4.3 The (a) top view and (b) 3-D view of the double chevron model. 42

4.4 Single buckle-beam actuator.. 43

4.5 The schematic drawings of the socket design in (a)
single chevron model and (b) double chevron model...................................... 46

4.6 FEA simulations of the opening of the sockets as a
function of the applied voltage of (a) single chevron
model and (b) double chevron model. 46

4.7 The schematic drawings of the micropart
(a) before assembly and (b) after assembly. 47

4.8 The cross-sectional view of the SOI wafer during fabrication. 48

4.9 The SEM photos of the fabricated devices. (a) A single chevron active lock. (b) A double chevron active lock. (c) A micropart. (d) A micropart with metal. 49

4.10 A schematic drawing of the assembled micropart using the active lock. 50

4.11 The assembly process. 51

4.12 The SEM photos of the assembled microparts. (a) Two micro parts are assembled in a row. (b) One micropart is assembled with the double chevron model. (c) One micropart is assembled with single chevron model. (d) The side view of one assembled micropart. ... 52

4.13 The plots of the deflection of the chevron actuator as a function of the applied voltage for (a) single chevron model and (b) double chevron model. 54

4.14 (a) The block diagram and (b) a photo of the force measurement setup. 54

4.15 Characterizes the force sensor. (a) The deflection as a function of voltage. (b) The force as a function of output voltage. 55

4.16 The plot of experimental spring constant at the tip of the force sensor. 56

4.17 Photos of the assembled parts with double chevron model being pushed by the force sensor. (a) The direction and location of the applied force by the force sensor. (b) Cross-sectional view of the force sensor pushing one assembled micropart. 57

4.18 The plot of the force applied on the assembled micro parts as a function of moving distance in (a) single chevron model and (b) double chevron model. 58

4.19 The solder coated (a) micropart and (b) socket.. 60

4.20 The force measurement on the soldered microparts. (a) The plot of the force applied on the assembled micro parts as a function of the moving distance of the motorized manipulator with and without heating. (b) SEM photo of an

assembled micropart with solder metal depositied on the contact area on the inserted finger and sidewall of the socket. 61

5.1 The design layouts of the (a) active lock for assembling the filter, (b) micromirror and (c) MEMS chip. 65

5.2 (a) A photo of inserting the filter into a socket with a vacuum gripper. (b) The assembled MEMS chip. 66

5.3 (a) The schematic drawing and (b) a photo of the optical measurement. 67

5.4 The plots of the transmission of the filters by direct measurement. 68

5.5 The measured (a) spectrum, (b) 3-dB bandwidths, and (c) 20-dB bandwidths of the assembled filters. 69

5.6 The measured (a) spectrum, (b) 3-dB bandwidths, and (c) 20-dB bandwidths of one assembled filter at 11 continuous angles. 70

5.7 (a) An SEM photo of one assembled microgripper using active joining mechanism. (b) A schematic drawing of an array of assembled microgrippers manipulating microparts. 74

5.8 The schematic drawing of a miniature micro spectrometer. 77

5.9 The SEM photos of an assembled micro helmet in the stadium of Dallas Cowboys……………………………………………79

LIST OF TABLES

Table Page

2.1 The parameters of layers in PolyMUMPs [2.3]. 14

2.2 Center frequencies and 3-dB bandwidths of the polymer filter........................ 30

4.1 The design parameters of single chevron model and double chevron model. ... 43

4.2 The parameters of single crystal silicon used in FEA. 44

4.3 The design parameters for the reaction force after assembly. 45

5.1 The optical performance of the unassembled filter chips. 68

5.2 The optical performance of the assembled filter chips. 69

5.3 Optical performance at different angles.. 71

5.4 Comparison of the optical performance.. 71

5.5 Force characterizations demonstrated experimentally...................................... 74

CHAPTER 1

INTRODUCTION

1.1 Motivation

Along with the development of micromachining technologies, microsystems have been demonstrated to augment the functionality of devices in telecommunication and sensor industries. Most evident work includes micromirrors for display and switches in fiber optics. A major of MEMS (Micro-Electro-Mechanical Systems) research is to develop complex systems integrated with IC, sensors and actuators. Integrating the entire optical system on a single chip has been one of the goals. An integrated system offers many advantages over conventional systems, including small sizes, light weights, more functionality and elimination of intermediate packaging and assembly steps. For example, known as micro-opto-electro-mechanical systems (MOEMS), in which integration and packaging of optoelectronic devices and passive optical components are always important issues to improve the system performance.

The key enabling architectures are the high-aspect-ratio three-dimensional structures with rigid mechanical interconnection and electrical interconnection with low contact resistance. System integration is a crucial issue due to the diversity of the sub-assembly and components. Hence it is indeed necessary to develop a reliable integration approach that allows the integration of heterogeneous microcomponents.

1.2 Research Objective

The objective of this research is to develop a general solution to achiever 3-D hybrid integration. In this work, two approaches are investigated for implementation of 3-D assembled microstructures: first, incorporating organic polymer with self-assembled polysilicon structures. The purpose is to combine the advantage of the good optical performance of the polymer with self-assembly architectures. Second, a new active joining mechanism is proposed and demonstrated by making the microcomponents on a SOI (silicon on insulator) wafer. Some 3-D structures are constructed by direct assembly technique.

1.3 Background: Assembly Technologies and Interconnection

1.3.1. Bonding

A wide range of bonding processes using various intermediate layers has been investigated, including: (1) anodic bonding, such as Si to glass; (2) fusion bonding, such as Si to Si; (3) glass frit bonding; (4) eutectic bonding, such as Si to gold covered Si; (5) solder bonding; (6) adhesive wafer bonding using polymers (non-hermetic).

MEMS components can be fabricated on different substrates and then can be transferred to another substrate through bonding. Several works have been demonstrated for wafer level and chip level stacking [1.1, 1.2].

The substrates are normally placed and clamped face to face, and then are bonded at elevated temperature. The placement of each microcomponent is predefined by wafer layout.

Some key requirements of the bonding process in general are: (1) precise alignment of the bonding structures on two substrates, (2) heating temperature and (3) pressure. The temperature varies for different bonding processes, such as anodic bonding is around 400°C. High pressure is typically desirable and provided by external load. Currently, there are commercially available wafer bonders and flip-chip bonders that can provide good alignment, heating and force in both the air and vacuum environments.

Once the two substrates are bonded, the substrate of the donor wafer is removed so that only the bonded device layer is remained on the other wafer. Both the dry and wet etch processes can be chosen to remove the substrate or the sacrificial layer according to the selectivity of different materials. If the MEMS devices are released before bonding and fixed by tethers on the donor wafer, the donor wafer can be removed by breaking the tethers [1.3].

Successful demonstrated works by this concept include: Single-crystalline silicon micromirrors bonded with polysilicon actuators for 2-D scanning [1.4], MEMS-based internal combustion engine [1.5], reflection-mode, integration of multiple-quantum-well (MQW) absorption modulators directly over active silicon CMOS circuits [1.6], etc.

The bonding technology is highly compatible with existing CMOS processes due to the planar "stacking" of the substrates. Multi-components fabricated on the same substrate can be assembled simultaneously by using this approach. Its limitation is that bonding occurs on the planar surface and requires a highly flatness for good bonding

quality. Otherwise the wafer/chip will be easily fractured due to the nonuniformity of stress distribution. In general, the heights of the bonded structures are all the same along *z*-axis. In other words, if the MEMS system is consisted of components with different aspect ratio to the substrate, flip-chip bonding or wafer bonding may not be used to assemble them. So bonding is called as 2 ½ -D assembly.

1.3.2. Self-Assembly

For self-assembly architectures, the objects, devices, and systems are fabricated on the same substrate and then 3-D structures are formed under the influence of external force. Two main approaches have been investigated by many researchers by using "Binding" sites and "Hinged" structure.

1.3.2.1. Binding Sites

In this technique, parts are freed from the substrate and randomly directed to the substrate that consists of binding sites at the desired location. The receptor binding sites on the substrate act as potential-energy wells for the shape matched binding sites on the microcomponents. Up to 1000 silicon chiplets were assembled by using vibration and gravitational forces [1.7], electrostatic force to locate and align the parts [1.8]. Single-crystal-mirror segments were assembled to surface-micromachined actuators by using the same concept with capillary force under water [1.9].

Both the dry and wet processes can be used under this approach. The parts and receptor binding sites can be fabricated on different substrate. The success of a self-assembly technique depends on the specific forces chosen for attachment and binding [1.10]. The most attractive thing is that thousands of microparts can be assembled

simultaneously which may lead to mass production. Different from flip-chip process, the parts are not aligned by the wafer layout. Instead, the path of motion to the destination binding sites is random. This random orientation of the parts is a big challenge for developing product level assembly method. After assembly, the parts are held by capillary force or adhesion temporarily. Lamination and heating solder metal were used to affix the parts permanently. Due to the planarity of the substrate, electrical interconnection can be patterned by photolithographic technique.

1.3.2.2. Hinged Structure

Another trend of assembly was demonstrated by the hinged structure. It allows the microcomponents such as actuators and mirrors to be predefined on the substrate and connected by hinge [1.11]. The out-of-plane motion on the microstructure can be achieved by activating the actuators with electrical connection, magnetic fields, or hinged like structures by heating up a coated polymer [1.12] and a solder metal [1.13].

This approach was demonstrated by several researcher using PolyMUMPs (Multi-User MEMS Processes), which is a commercially available standard fabrication process. The monolithic fabrication process allows precise positioning of optical components on the same chip. Micro-optical devices such as switches [1.14, 1.15], scanning mirrors [1.16], reconfigurable grating [1.17] and free-space optical bench [1.18] have been demonstrated.

Polysilicon, as the structural material, is typically fabricated by low pressure chemical vapor deposition (LPCVD) process followed by doping and annealing. It has inherent scattering and significant absorption properties in visible and near infrared

(NIR) ranges [1.19, 1.20] as an optical interface and it also has a high electrical resistivity. Accordingly, the functionality and performance of an assembled system are limited by the material property of polysilicon. Attempt of integrating single-crystalline and polysilicon was explored through bonding, in which a single-crystalline silicon wafer as the optical interface and a polysilicon substrate as the actuation layer were bonded together in order to provide good optical performance with the polysilicon actuators [1.4].

1.3.3. Direct Assembly

In direct pick and place assembly, the devices can be fabricated on separate substrate. A precisely controlled robotic assembly station is utilized to manipulate (pick up, orient and place) the microparts. It's similar to the assembly line in macro world. As the assembled parts are in micrometer to millimeter range in size, forces should be dramatically reduced according to this scaling. Adhesion forces between the end-effecter, such as microgrippers and a micropart, become significant compared to a gravitational force when the microparts are less than one millimeter in size [1.21]. Therefore the interfaces between the end-effecter and the microparts, also between the microparts and substrate or sub-assembly have to be carefully designed with the consideration of interaction forces. If the mating force is too large, it may cause the fracture of the microgrippers and the microparts.

The most essential procedure of this assembly is the reliable 90 °rotation of the part out of the plane. Zyvex Corporation is actively pursuing the automated, multi-degree of freedom (DOF) robotic assembly system with microgrippers [1.22]. They also

demonstrated an experimental assembly [1.23, 1.24]. Dechev developed a 5-DOF robotic assembly station and manipulated the assembled parts with microgrippers that mounted on a solder head [1.25]. A 3-D air-core-inductor was constructed by this process [1.26]. Different from previous two approaches, UC Berkeley used an orthogripper to grasp and rotate the microparts simultaneously instead of using a macro scale rotation stage to perform the out-of-plan rotation,. Out-of-plane motion was demonstrated by pushing the assembled structure with an in-plane comb drive actuator [1.27].

The cost of direct assembly remains high due to the robotic assembly station. The argument of this approach is mainly focused on the assembly throughput and the time reduction by decoupling fabrication processes.

1.3.4. Interconnection

There are many challenges to interconnect MEMS structure with traditional IC circuits or other type MEMS structures. Among them, a key challenge is the integration of electrical and mechanical functions.

For assembled chips, multilevel wiring and etch-through-via can be used to connect the chip with electrical circuits. When connecting a single device to another structure, it is very difficult. In the micro world, it's unlikely to fabricate a screw shape connector with current fabrication constraints. Mechanical fasteners have been developed to form the interconnection of mechanical parts and various mechanical fasteners have been demonstrated.

“Micromechanical Velcro” was built and characterized [1.28]. These structures have arrays of SiO_2 caps on silicon pedestals and were used for wafer bonding and piercing biologic tissues [1.29]. Snap fasteners based on latching mechanism were first used as in plane interconnection between microstructures [1.30]. Later, it was used as vertical plug-in connectors and the 3-D assembled jammer and mirrors have been demonstrated by Zyvex [1.23]. A wedged connector was designed to fix the micropart by sticking a 5μm wedge into the small gap below the device layer on the socket [1.31]. A clamping lock connector consists of a wedge and a triangular clamp with an angled surface. The micropart is inserted between the triangular clamp and the rigid device layer and is held by frictional force [1.27].

All the approaches above suffer from two main constraints. First is the geometry of microparts. For a snap lock, it requires spring arms or cantilever beams on either the socket or the assembled parts or both. The wedge connector requires a thin arm to be able to insert it into the gap. This constraint limits the selection of materials for assembly. Silicon and polysilicon can be patterned by DRIE or surface micromachining, while other materials, such as glass and ceramic, are very difficult to achieve such specific shapes. Second constraint is that the matting forces between the connector and sockets, between the micropart and end-effectors, should be carefully determined. Otherwise, it may cause the fracture of the connectors or the end-effectors.

1.4 Thesis Overview

Chapter 2: Describe the hybrid material integration through a polymer based thin-film filter with self-assembled microstructures. First the self-assembly platform,

PolyMUMPs, is briefly introduced. Then the mechanical design and optical design are presented followed by the challenges of incorporating the polymer, the fabrication and characterization of the fabricated devices. Finally, the advantages and drawbacks of this integration approach are discussed.

Chapter 3: Introduce direct assembly technique, the overview of the assembly requirement and the 3-D assembly system used to perform the assembly tasks.

Chapter 4: Introduce a new active joining mechanism for assembling 3-D MEMS structures. The design concept, architecture, features of the active lock, and the module features of the micropart are presented. The fabrication process and the assembly procedure are investigated. A few 3-d structures are constructed by direct assembly and the performance of the active lock is characterized.

Chapter 5: Two applications of utilizing the active locking mechanism are investigated. First, one conceptual DWDM (dense wavelength division multiplexing) with two filter channels is assembled using active locks. The interconnect design is presented and the filters are characterized. The purpose is to combine the advantages of the good performance of the multi-layer thin-film filters and the precisely aligned MEMS structures. Second, the parallel assembly versus serial assembly techniques is discussed. Potentially applications are illustrated.

Chapter 6: Summarize the work in this dissertation.

1.5 Thesis Contributions

There have been six contributions from this thesis in the area of assembly of MEMS devices and the area of MEMS device design, which include:

1. The development and fabrication of a polymer-based micro filter with self-assembly structure. We have shown low losses in the optical signal processing and feasibility of building a thin-film Fabry-Perot filter.
2. The development of a novel joining mechanism which can be used for constructing in plane and out-of-plane microstructures. Benefits of microassembly by means of an active locking mechanism include: (1) microassembly tools do not require providing large mating forces, which often cause fractures of microgrippers. Zero insertion force of joining the microparts to the active lock has been demonstrated. (2) The active lock is independent of the function of microcomponents. It accommodates to microparts made of various materials, dimensions and shapes. (3) Self-aligned microstructures have been achieved by prearranging the location of the microparts on the chip. (4) Misalignment can be corrected by opening the lock and adjusting the microparts.
3. The ability to apply voltage to the active lock, after the micropart has been assembled, and replace the micropart without damage the socket.
4. The development of a high force (about 40 mN) to disengage the microcomponent from the socket. It highly improves the reliability of the joining and the stiffness of the assembled microstructures. It can be used for several MEMS applications and possibly to form complex multi-link microstructures, such as micro robot.
5. The impact on free-space optical applications through the demonstrated DWDM filters. This easy assembly process with precisely optical alignment is cost effective

and results in very low insertion losses, which are beneficial for packaging optoelectronic components.

6. The potential capability of forming a good electrical interconnection and a rigid mechanical connection simultaneously by flusless soldering, which may enable out-of-plane actuation of the assembled microstructures.

CHAPTER 2

HYBRID MATERIAL INTEGRATION BY SELF-ASSEMBLY

2.1 Methodology

PolyMUMPs is the industry's longest-running MEMS multi-project wafer service. It has driven the idea of the standard process approach as a clear path to device functionality and volume production. The monolithic fabrication feature allows precise positioning for many optical components on the same chip. Micro-optical devices such as switches [1.14, 1.15], scanning mirrors [1.16], and reconfigurable grating [1.17] have been demonstrated. While implementing the transmission-type components, such as fresnel lenses [2.2], one faces serious technical challenges. The reflection-type devices do not suffer from the characteristics of the polysilicon as they utilize metal coating on the silicon layer to reflect light. The transmission-type devices, however, suffer from the high absorption of visible or near-infrared signals in polysilicon. Therefore the inherent material properties of polysilicon make it not suitable for transmissive type optical devices.

Polymers have been considered as one of the most versatile materials in making optical devices for communication and sensor applications. They provide good optical transparency to form filters, lens and many optical components with ease of fabrication. They are scalable and compatible in dimensions with requirements in optics and can be

fabricated on inorganic substrates, such as silicon and quartz. In this chapter, a new approach by integrating polymers on silicon-based MEMS devices is proposed. The motivation is to combine the advantages of demonstrated silicon-based MEMS actuators and excellent optical performance of polymers. This idea is demonstrated by a polymer-based out-of-plane Fabry-Perot filter which is assembled by scratch drive actuators. In the filter design, organic compound material is applied on the silicon-based framework within the optical signal propagation path to form the optical interfaces. The challenge lies in incorporating the polymer into PolyMUMPs structure during the post fabrication process.

PolyMUMPs is introduced in section 2.2. The optical filter design, including mechanical and optical design, is presented in sections 2.3 and 2.4. The fabrication issues and processes are illustrated in section 2.5. Finally the results are presented in section 2.6.

2.2 Introduction of PolyMUMPs

PolyMUMPs is a three-layer polysilicon surface micromachining process, with two sacrificial layers and one metal layer. Eight mask levels create 7 physical layers (Table 2.1). The minimum feature size in PolyMUMPs is 2 μm.

The MUMPs process starts with 150 mm n-type wafers of 1-2 Ω-cm resistivities. The seven layers are deposited and patterned sequentially. After that, the wafers are diced into 1 cm by 1 cm chips followed by removing the oxide sacrificial layer in concentrated HF (49%).

Table 2.1 The parameters of the layers in PolyMUMPs [2.3].

Material Layer	Thickness (μm)	CD Tolerances	Lithography Level Name
Nitride	0.6	--	--
Poly 0	0.5	1.800 to 2.200 um Lines	POLY0 (HOLE0)
First Oxide	2.0	1.800 to 2.200 um Spaces 1.700 to 2.300 um Spaces	DIMPLE ANCHOR1
Poly 1	2.0	1.750 to 2.250 um Lines	POLY1 (HOLE1)
Second Oxide	0.75	1.750 to 2.250 um Spaces 1.750 to 2.250 um Spaces	POLY1_POLY2_VIA ANCHOR2
Poly 2	1.5	1.700 to 2.300 um Lines	POLY2 (HOLE2)
Metal	0.5	2.500 to 3.500 um Lines	METAL (HOLEM)

The mask layout for each layer is drawn by a software, MEMS Pro. Because PolyMUMPs is a standard process, the thickness of each layer is known as a fixed value. Only 2-D layout needs to be drawn for each layer and 3-D model can be viewed through the 3-D model tools.

2.3 Microcomponent Design

2.3.1. Scratch Drive Actuator

Scratch drive actuators (SDA) [2.4, 2.5] are a step-motion microstructure which moves by an electrostatic driving mechanism. A scanning electron microscope (SEM) picture of SDA is illustrated in Fig. 2.1 (a) and its schematic drawing is in Fig. 2.1 (b). It's composed of a top plate and a bushing. There is an insulation layer between SDA and the substrate. In this work, the SDA is made by polysilicon, substrate material is silicon and silicon nitride is used as the insulator. The cross-sectional view of the step motion of the SDA is shown in Fig. 2.1 (c).

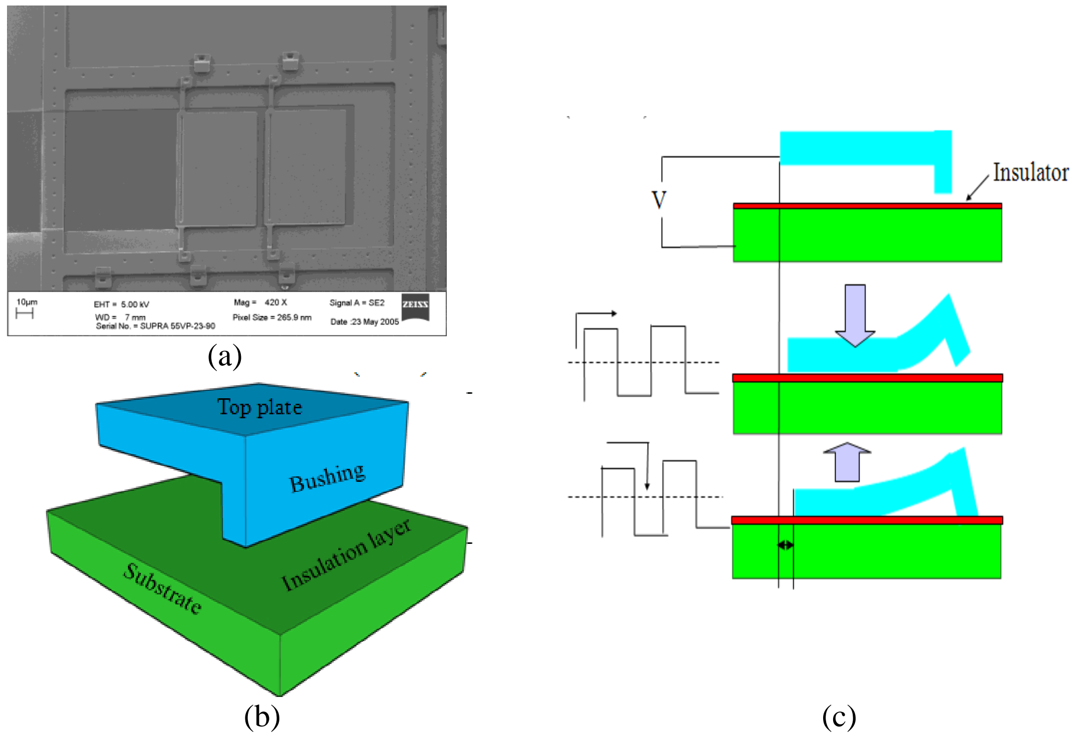

Figure 2.1 (a) A SEM photo, (b) a schematic drawing and (c) a step motion model of the scratch drive actuator.

2.3.2. 3-D Hinge

The 3-D hinge design follows the methodology in [2.6, 2.7]. It's made of two polysilicon layers (Poly1 and Poly2) and can be folded out of the plane. Two types of hinges are utilized to assemble microstructures. Figure 2.2 (a) shows a fixed hinge. It consists of one arc and a rotation bar. Both ends of the arc are attached to Poly0 and the center part forms a 4.75 μm gap on top of Poly0 which is an immovable layer in MUMPs process. The arc is made by Poly2. The 2 μm thick rotation bar made by Poly1 is laid within this arc which enables the rotation of the part that connected to the bar. A cross-sectional view of this fixed hinge is illustrated in Fig. 2.2 (b).

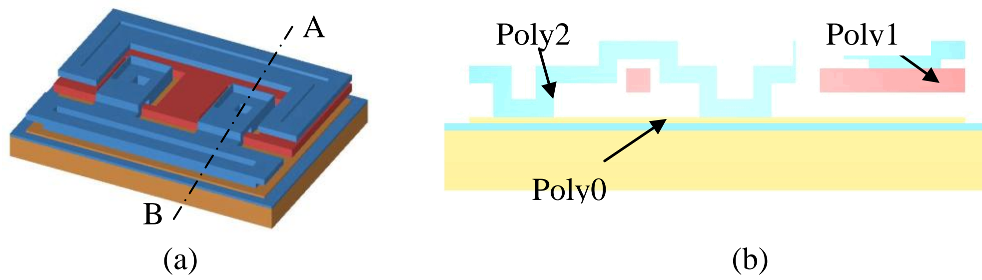

Figure 2.2 (a) 3-D model of the fixed hinge. (b) The cross-sectional view along the line A--B.

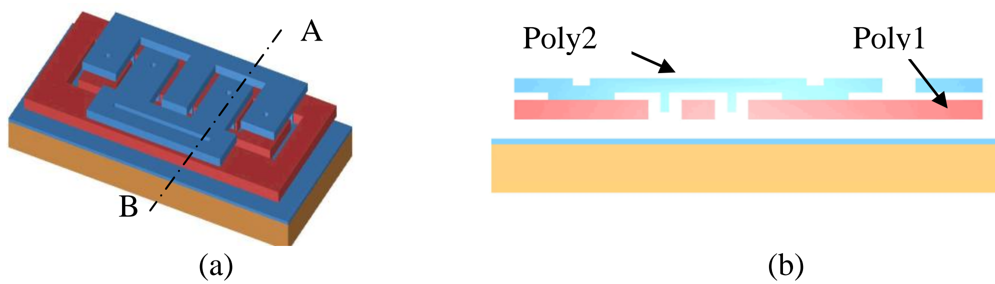

Figure 2.3 (a) 3-D model of the movable hinge. (b) The cross-sectional view along the line A--B.

As shown in Fig. 2.3, the movable hinge is similar to fixed hinged but the arc is attached to Poly1 instead of Poly0. Since Poly1 layer is movable after release the sacrificial oxide, this hinge can be used for connecting actuators and microstructures through Poly1. The actuation from the actuator can result pull, push or lift-up motion on the connected microstructures.

2.4 Filter Design

2.4.1. Mechanical Design

The self-assembly architecture is composed of actuators and a hinged support frame for the polymer, as shown in Fig. 2.4 (a) and (b). The step motion of the scratch drive actuators (SDAs) can be controlled by applied voltages. The SDAs move along a

straight path with applied voltages and the motion is directed by the guiding rails. The hinges translate the lateral force to a rotation one for out-of-plane assembly, as shown in Fig. 2.4 (c) and (d).

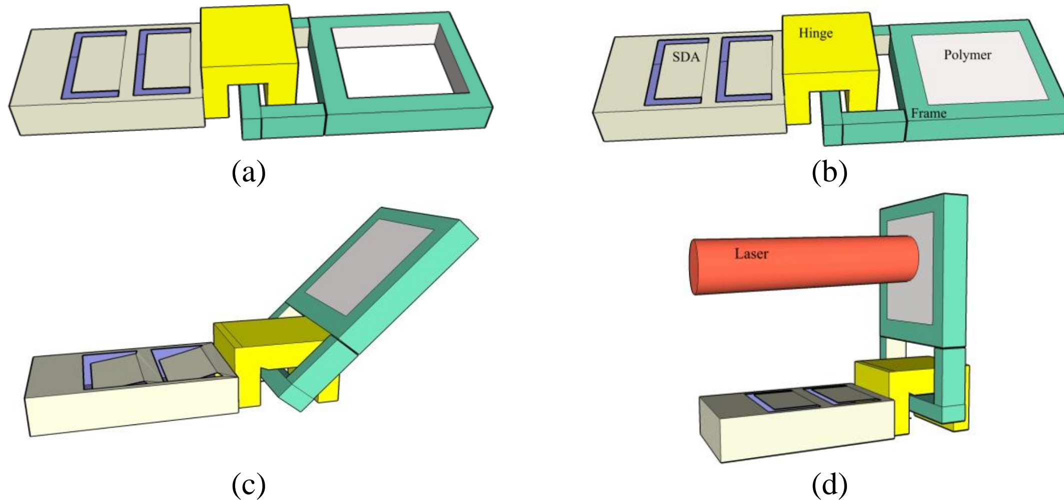

Figure 2.4 Device architecture of the micro filter. (a) The SDA is connected to the hinged polysilicon frame without polymer coating. (b) Polymer film acts as the optical interface supported by the polysilicon frame. (c) The step motion of scratch drive actuators lifts the frame up. (d) The frame pivots out of plane and stands perpendicularly to the substrate after assembly with an incident laser shone normal to the filter surface.

The hinge, actuators and optical design follow the system assembly methodology discussed in [2.7]. The scratch drive actuator design has been demonstrated in our previous work [2.8]. A circular inner frame made by a polysilicon layer (Poly1) forms a support frame for the polymer attachment while the outer one connects to the mechanical structure for actuation (Fig. 2.5). During assembly, the support frame together with the polymer layer will be lifted up and rotates out of the plane. A laser beam with a propagation axis parallel to the substrate surface incidents on

and passes through the polymer surface. The frame design should accommodate the optical beam size.

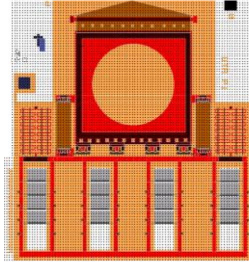

Figure 2.5 Physical layout of the assembly structures.

2.4.2. Optical Design

A thin-film Fabry-Perot interferometer, composed of two parallel interfaces separated by a distance, as shown in Fig. 2.6, was designed. Two types of optical interfaces are considered: all-dielectric and metal-dielectric types. In all-dielectric type, stacking multiple high and low refractive index material layers alternatively can achieve the required filter shapes with high transmission in passbands. However, the all-dielectric multiple layers may need a large number of stacking and result in a very thick optical interface. The thickness may exceed the thickness of the polysilicon frame on the MEMS chip, which makes the assembly process difficult. The large numbers of stacking also make the photolithography and patterning processes complex and cost prohibitive.

In a metal-dielectric filter, metal layers serve as the high index layers. The thickness of each metal layer is less than 100 nm and the very high index reduces the numbers of layers required. Both factors dramatically reduce the filter thickness. In our

feasibility demonstration, we chose to deposit one layer of metal on each side of the polymer to form a (high-low-high) Fabry-Perot filter.

The transmittance spectrum of a Fabry-Perot etalon is determined by

$$T = \frac{I_0}{(1-R)^2 + 4R\sin^2(kl)} \tag{2.1}$$

where T is the flux density of transmitted wave, I_0 is the flux density of the incoming wave, R is the reflectivity at mirror surfaces, l is the distance of the gap between plates, and the wavenumber k is defined as

$$k = \frac{2\pi}{\lambda} \tag{2.2}$$

where λ is the wavelength. The frequency spacing, or the free spectral range (FSR) of the transmission bands depends on the gap and the spectral shape of each passband depends on the reflectivity R. The reflectivity of the optical interface is determined by the refractive index of the material forming the cavity, if there is no coating on the cavity surfaces. The reflectivity could also be varied by thin-film metallic coating to achieve a desired filter spectral shape.

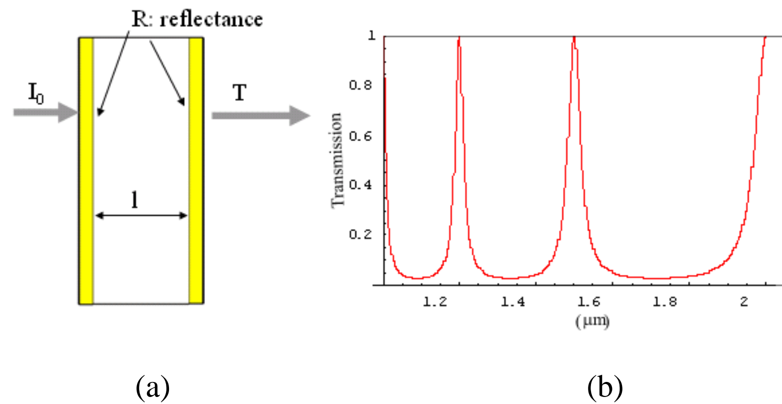

(a) (b)

Figure 2.6 (a) A Fabry-Perot etalon. (b) The transmittance spectral shape.

To compare optical performance, simulations of the filter with different cavity materials such as polymer and single-crystal silicon were investigated. Intrinsic single-crystal silicon presents good optical quality [2.9]. However, it possesses challenges of integration with the polysilicon MEMS actuators without expensive fabrication processes. The same cavity thickness with the same thin-film of gold coated on both sides of the polymer or silicon is assumed in the simulations. Figure 2.7 shows the filter shapes with a (a) 3 μm and (b) 10 μm cavity. With a refractive index of 1.92 of the polymer [2.10], the loss in the polymer filter is as low as the single-crystal silicon. The difference in refractive index of the polymer and silicon results in different passband frequencies and bandwidths. Both parameters, however, can be varied by choosing a proper metallic coating on the surfaces.

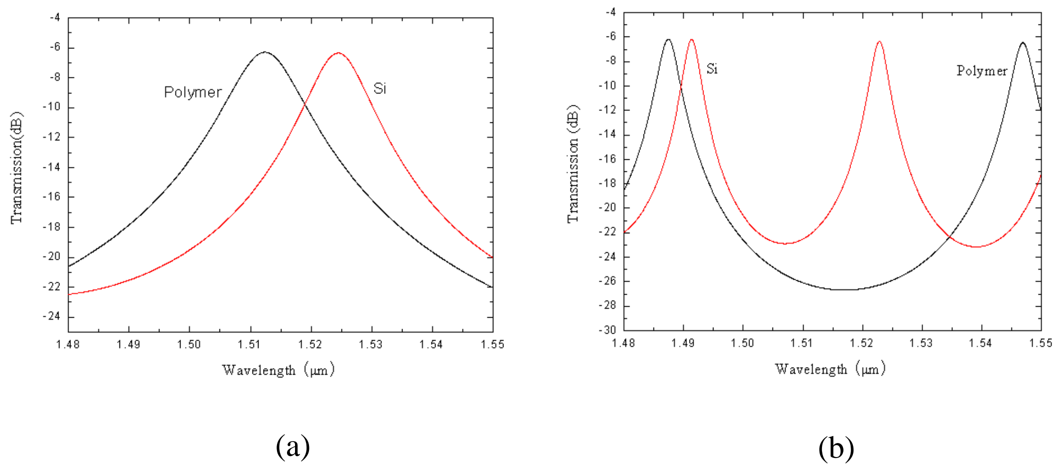

(a) (b)

Figure 2.7 Simulation results of the Fabry-Perot etalon with polymer and Si cavities. The cavity thicknesses are (a) 3 μm and (b) 10 μm, respectively.

2.5 Fabrication

2.5.1. Challenges

The optical components require a relatively large surface area to accommodate the light propagation. This presents a fabrication issue for the optical design. HF (Hydrofluoric acid) is used to remove the sacrificial oxide layer to release the MEMS structures before assembly. In order to expedite the releasing process and avoid over-etching problems, etching holes are commonly utilized on the polysilicon layers, especially for large structures. For a reflective MEMS mirror, the etching holes will introduce excessive transmission losses of the reflected optical energy [2.11]. For our filters, the etching holes on the polymer layer are also undesired since the phase fronts of the optical signal will be distorted. With considerations and tradeoffs in the optics and MEMS designs, the diameter of the optical surface is chosen to be 450 μm. The center of the optical axis is 305 μm above the substrate. We include 16 scratch drive actuators to actuate the silicon frame. Spring structures are included in the mechanical design to provide counter forces to the pulling ones in order to correct the pulling accuracy. In the case of over actuation, the springs will push the structure in the opposite direction. Once located in the desired position, the actuation is stopped and mechanical locks could secure the mechanical integrity. In this work, we include etching holes in the silicon layers but not in the polymer layer. The consequence then is an extended etching time.

2.5.2. *Choosing Polymer*

It is critical to choose the proper polymer to satisfy both mechanical requirements and optical performance. There are a wide variety of polymers suitable for optical applications. To be compatible with 3-D MEMS structures, we are interested in polymers that can offer: (1) good optical transparency at the 1.55 μm wavelength range, (2) surface uniformity, (3) resistance to hydrofluoric acid (HF) and solvents like acetone or IPA for the polymer to survive after the post processes and the chip release, (4) good adhesion to polysilicon, (5) a low coefficient of thermal expansion and good mechanical properties, and (6) easy fabrication procedures.

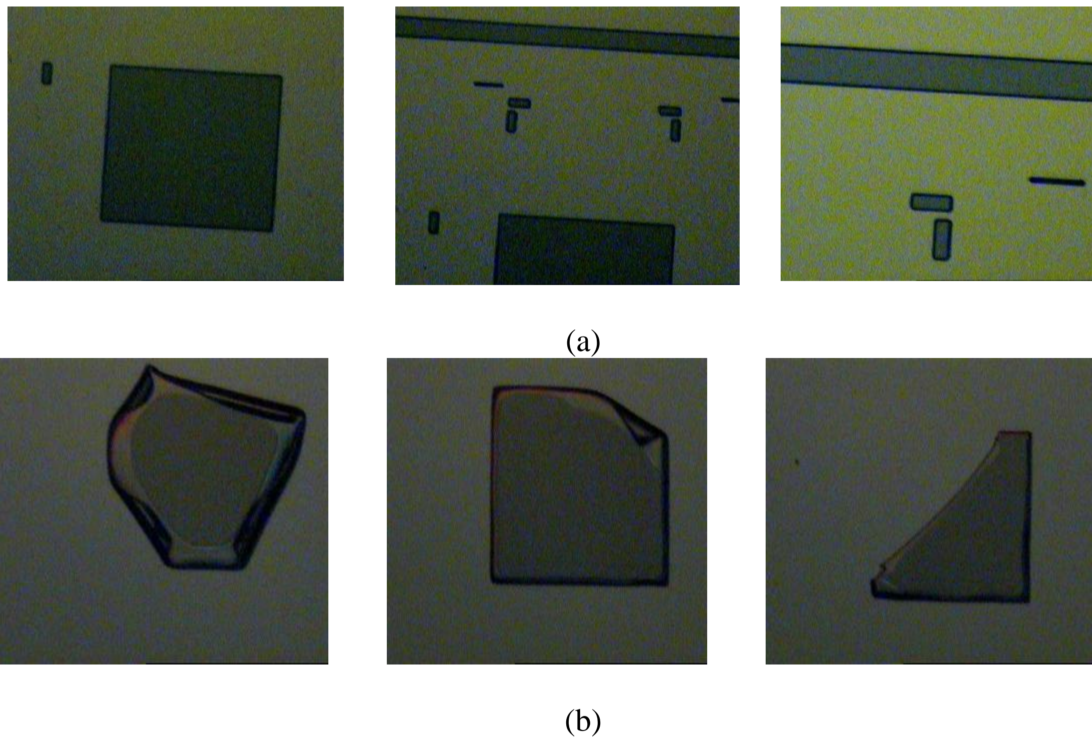

(a)

(b)

Figure 2.8 The microscope pictures of PirlIII patterns (a) before and (b) after release.

Several organic materials, such as S1808, AZ2020, PirlIII and PI2737, have been investigated in the post fabrication process. All the polymers are first processed on a 2 inch silicon wafer to explore whether they can survive in the chemicals. Most of them (S1808, AZ2020, PirlIII) loss the original patterns after the release procedure. Figure 2.8 shows the microscope photos of polyimide PirlIII before (Fig. 2.8 (a)) and after (Fig. 2.8 (b)) release.

As shown in Fig. 2.8 (b), the corners of the big polymer film (450 μm x 450 μm in square shape) are lifted up and the small patterns are all peeled off after release. The adhesion of this polymer to silicon substrate is poor after being attacked by HF and acetone. Among them, PI2737 is the only one that can survive after the release procedure with good patterns. More details about PI2737 will be presented in the following sections.

2.5.3. Fabrication process

As it was mentioned previously, the support frame and actuators are fabricated by the foundry service PolyMUMPs. The physical layout is made in consideration of post processes in mind including polymer attachment positions and alignment marks. The subsequent fabrication process starts with partially removing the phospho-silicate glass (PSG) layer on the MEMS chip in buffered oxide etch (BOE). Photoresist is spin-coated then patterned to define the filter area on the polysilicon frame, as shown in Fig. 2.9 (a). In order to achieve a flat surface on the filter, PSG within the filter area is etched to the depth where the inner framework is exposed (Fig. 2.9 (b)). Adhesion promoter solution is applied on the chip surface to improve the adhesion strength

between the polymer layer and the polysilicon frame. The chip is first flooded with the promoter solution for 20 seconds then spin at 2500 rpm for 30 seconds. Then PI2737 polymer layer is spin-coated and patterned by photolithography to form the filter structure (Fig. 2.9 (c)). After a soft bake at 65 ^{o}C for 3 minutes and a hard bake at 95 ^{o}C for 5 minutes on a hot plate, the polymer is cured in the oven at 260 ℃ for 3 hours (Fig. 2.9 (d)). The remaining PSG on the MEMS chip is removed by BOE, as shown in Fig. 2.9 (e). Finally, acetone and isopropyl alcohol (IPA) are used to reduce the stiction between the movable structures and the substrate.

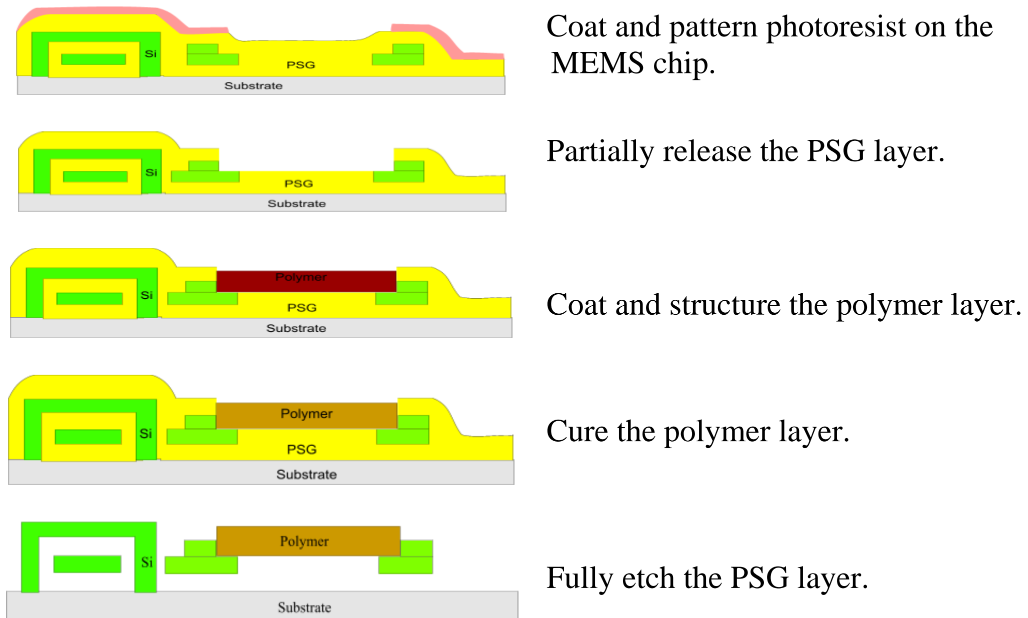

Figure 2.9 Cross-sectional views of the micro filter in post fabrication processes.

2.6 Results

2.6.1. Fabrication Result

The UV patternable polyimide PI2737 shows high compatibility with our processes. The exposed areas are cross-linked and become insoluble. The sequential

cure heating cycle converts the polyamic ester to the insoluble imide form and drives out remaining solvent. The coefficient of thermal expansion (CTE) of 16 ppm/^{o}C [2.12] is lower than most of other polymers, such as SU-8 with 52 ppm/℃ [2.13] and bisbenzocyclobutene (BCB) with 52 ppm/℃ [2.14]. Therefore, there is no obvious shrinkage of the cured polymer film on support frame surface, as shown in Fig. 2.10 (c), comparing to the after-soft-baked one, as shown in Fig. 2.10 (b). The polymer film also demonstrated its resistance to BHF as it does not show wrinkles on the polymer surface in Fig 2.10 (d). An SEM picture of the support frame with polymer layer is shown in Fig. 2.11.

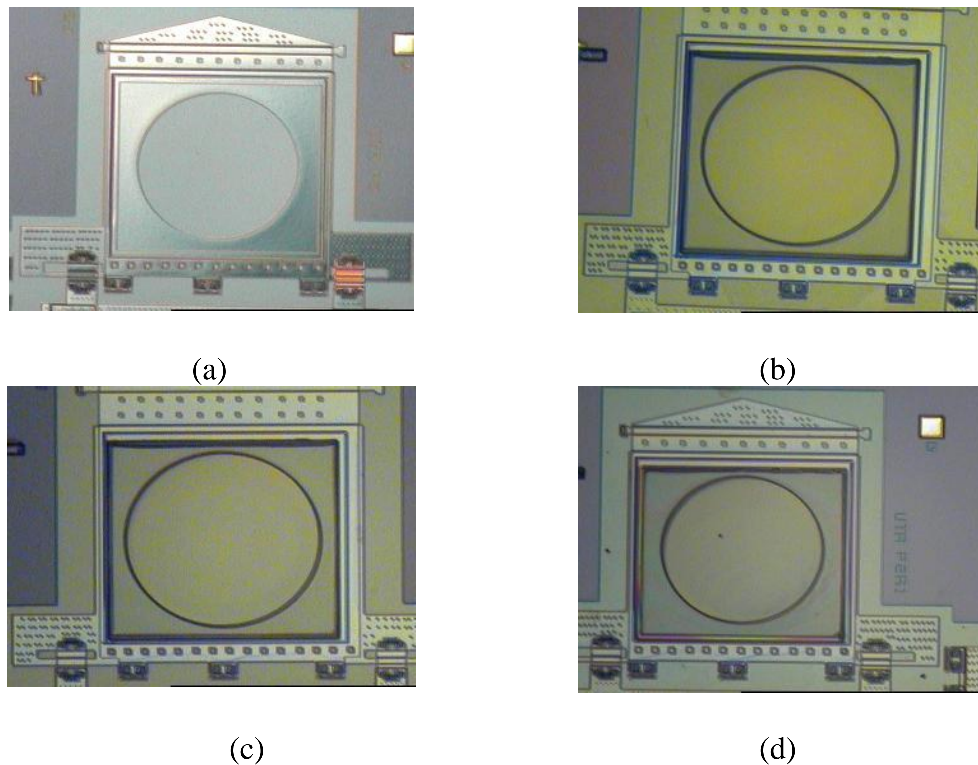

Figure 2.10 Microscope photos when process the filter device during post fabrication. (a) The MEMS chip without applying polymer. (b) After coating polymer on the polysilicon support frame. (c) After the curing procedure. (d) After releasing the chip in BOE.

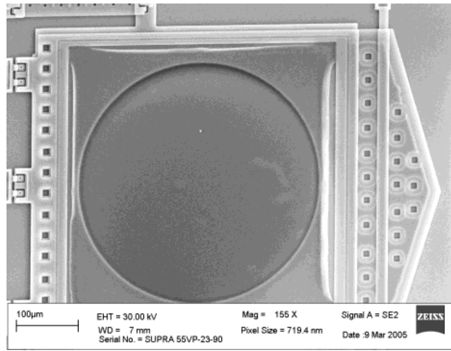

Figure 2.11 SEM photo of the polysilicon support frame coated with the polymer film.

2.6.2. Material Property and Characterization

The polymer PI2737 offers very low absorbance in the wavelength range from 500 nm up to 2000 nm nominally [2.15]. In order to confirm the results, we measured the absorption coefficient of the cured polymer on glass slides with a *JA Woollam* optical ellipsometer to verify the absorption coefficient. The thickness of the polymer is 3 µm. Given the instrument only provides a wavelength range from 300 nm to 1000 nm, the measure result shows insignificant absorption in the range from 500 nm to 1000 nm, with a slight increasing trend as the wavelength increases (Fig. 2.12).

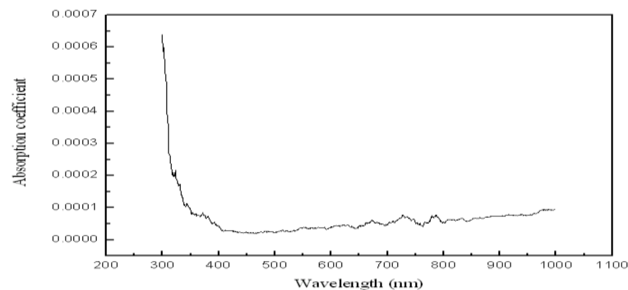

Figure 2.12 The plot of the measured absorption coefficient of PI2737.

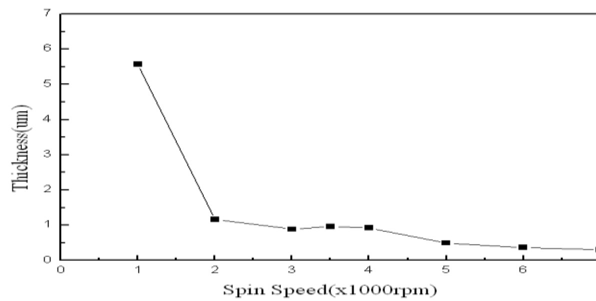

Figure 2.13 The plot of the thickness of the cured polymer film as a function of spin speed.

Since the thickness of the polymer film determines the free spectral range (FSR), the thickness of the cured polymer as a function of the spin-coating speed has been investigated. The thickness of the polymer film was measured by a *TENCOR* profilometer. The PI2737 polymer was spin-coated with different speeds on glass slides and cured in an oven at 260 ^{o}C for 3 hours. Fig. 2.13 shows the results for spin speeds varied from 2000 rpm to 7000 rmp.

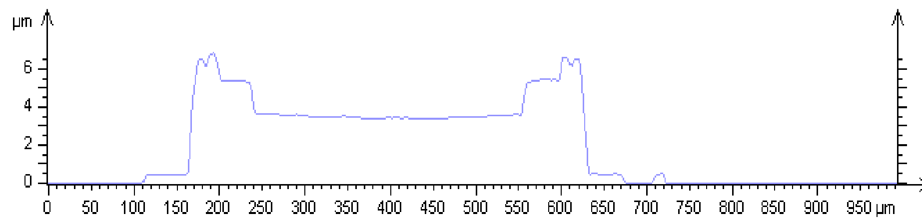

Figure 2.14 The plot of the measured surface profile of the cured-polymer filter.

2.6.3. Assembly Result

The released MEMS chip is placed on top of a 3-D stage. Two micro manipulators connect with the power supply are mounted on a fixed stage next to the chip. When applying voltage across the contact pads, the scratch drive actuators will be activated. The scratch drive actuators are biased with 53.5 V signal and push the support

frame out of plane. The actuation distance can be monitored by the biasing pulse numbers to make sure the filter is standing perpendicularly to the substrate. Figure 2.15 shows a scanning electron microscopy photo of the assembled result. The polymer shows very good mechanical property.

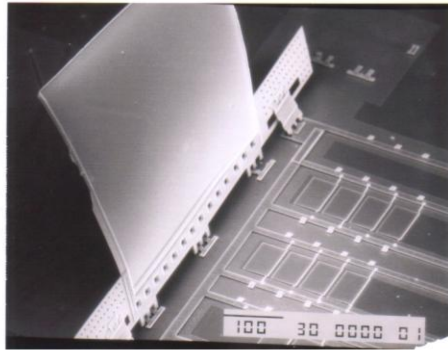

Figure 2.15 An SEM photo of the polymer filter supported by the MEMS frame and actuators.

2.6.4. Optical Measurement

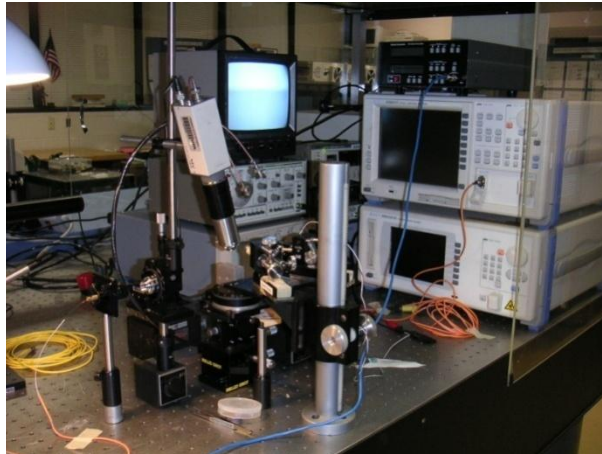

Figure 2.16 A photo of the experimental setup.

As it was mentioned previously, to characterize the optical performance of the filter, the MEMS chip is mounted on a 3-D stage. Biasing voltage is applied on the

contact pads to actuate the scratch drive actuators. The frame is then pushed up and the filter stands up perpendicularly to the substrate.

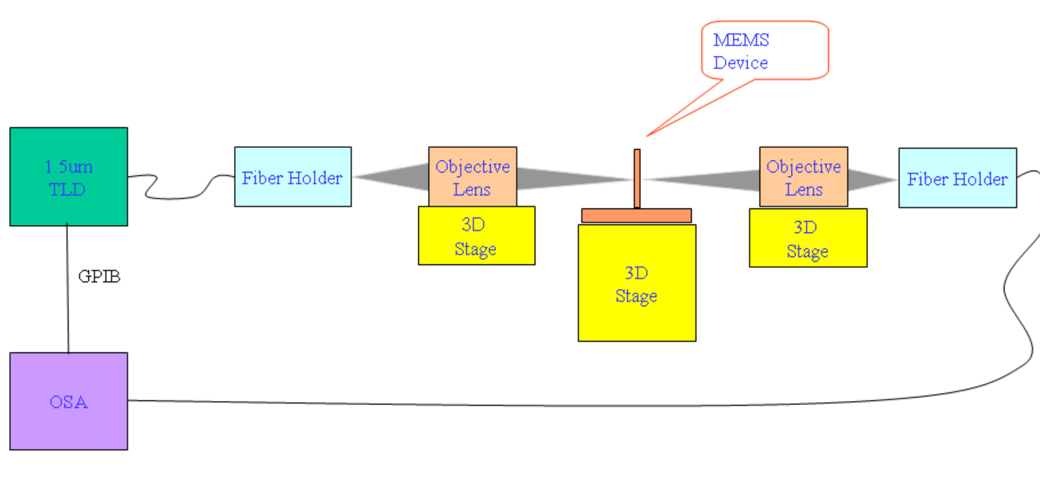

Figure 2.17 The configuration of the optical measurement.

A tunable laser diode (TLD) is connected to the optical spectrum analyzer (OSA) to synchronize frequency sweeping between 1480 nm and 1580 nm. The laser from TLD is coupled into a single-mode fiber fixed on a fiber holder. Then the light is shone on to the objective lens to adjust the focus beam size that illuminates on the polymer filter surface. Another objective lens is used on the other side of the filter to couple the transmitted light into another single-mode fiber connecting to the OSA. The calibration is done by moving the MEMS chip out of the optical path. The insertion loss from the optical setup is then calibrated out. The filter diameter is 450 μm and two objective lenses are fine-tuned to reach a desired laser beam size. The insertion loss of the polymer interface is less than the noise levels so that we could not precisely characterize it. The reflectivity is also low due to the low refractive index of the polymer. The low reflectivity results in a very broad spectral shape for each resonant

peak. Consequently, the etalon spectral characteristics are not obvious. This, however, is beneficial to our design since it verifies the low loss and low refractive index of 1.92.

We sputtered a thin layer of gold on the polymer surfaces to achieve a higher reflectivity on the Fabry-Perot surfaces. The theoretical and the measured data of transmission are shown in Fig. 2.18. The center frequencies and 3-dB bandwidths are listed in Table. 2.2. The experimental curve is lowered to show the matched spectral shapes. The insertion loss is still insignificant. The curves show the measurement matches with the theory within some discrepancy in the shapes. It may be due to the thin-film metal coating. The reflectivity of thin-film gold may vary significantly due to different fabrication conditions and quality.

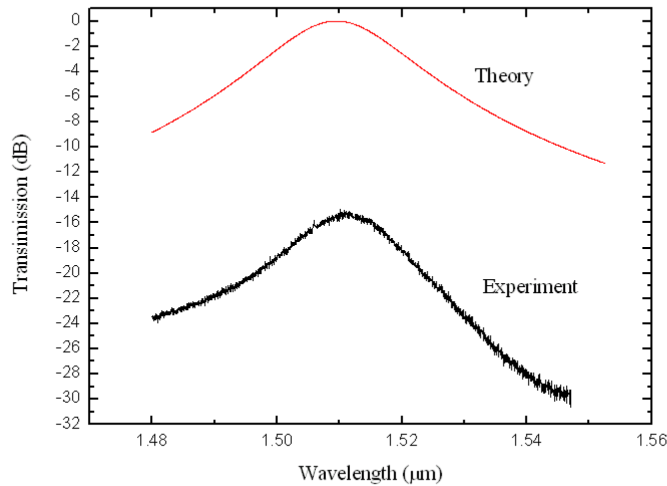

Figure 2.18 The plot of theory and experiment data of transmission spectrum.

Table 2.2 Center frequencies and 3-dB bandwidths of the polymer filter.

	Center Frequency f (THz)	3-dB Bandwidth (THz)
Theory	198.4	196.7 – 200.1
Measurement	198.6	197.4 – 199.7

2.6.5. Summary

In summary, PolyMUMPs has demonstrated the feasibility and flexibility of material integration. Organic polymer has been successfully integrated with traditional polysilicon self-assembly microstructures. A new device, a polymer based thin-film filter, has been designed and fabricated. It's compatible with existing device such as mirrors and switches and sharing a common platform.

We have shown low losses in the optical signal processing and feasibility of building a thin-film Fabry-Perot filter. The filter shape is demonstrated. However, for a filter with very narrow passband, additional optical coatings to enhance the performance are required. If the coating material is not as the same material of those already known in this process, the effort of evaluating and incorporating the new materials is going to be repeated every time.

This approach may be suitable for making a single type device with easy post fabrication procedure. As for a system requires various materials, the obstacles that prevent to achieve the goal through fabrication lie in: (1) the material compatibility and current fabrication constraints. (2) Substitute material can be used but it may affect the performance of other components in the system. Other than this, the heterogeneous architectures dramatically increase the complexity and cost of developing fabrication process. (3) The defect of individual component may affect the integrity and performance of the system.

Considering the reasons mentioned above, we explore another approach by using direct assembly.

CHAPTER 3

INTEGRATION OF MICROCOMPONENTS BY DIRECT ASSEMBLY

A more general, direct pick and place microassembly approach enables the integration of microcomponents fabricated in several different processes. Several out-of-plane structures were constructed successfully by using direct assembly technique. For pick and place microassembly, it is essential to develop microparts which can be picked up and parts (called sockets) into which these microparts can be assembled. Conventional types of fasteners such as screws and nuts are not suitable in microassembly because of their complicated structures and motions. The scaling of forces at the micro scale makes the use of conventional fasteners even more difficult [1.31]. Thus a new "general" joining mechanism is demonstrated in this thesis by using in-plane actuators to serve as the interface to assembled microcomponents. Direct assembly technique has been chosen for integrating microcomponents fabricated on an SOI wafer in this work. The 3-D microassembly station will be introduced first followed by a brief overview of the assembly process.

3.1 The Overview of Assembly Requirement

The general requirements for direct assembly are: (1) a microassembly system of which the movements can be precisely controlled. (2) End-effecters that mounted on the robotic station to the interface with the micropart perform manipulations, such as

grasp and release. (3) The microparts and sockets can be fabricated on different substrates. The micropart contains features to interact with the end-effecters and features to join other components or sub-assembly.

The procedures of assembling microparts are limited by the following factors: first, the final configuration of the assembled microstructures is determined by the interface of sub-structures. Second, the design of the end-effectors and manipulators should be able to perform the required manipulation task on microparts, including, grasping, placing, pushing, dropping, etc. Third, in most demonstrated direct assembly, the end-effectors exert force on micropart in order to enforce insertion and interface. Hence, microgrippers have been designed to provide compliant in and out of plane forces with capability of picking a range of different parts [3.1]. Other end-effecters can also be used, such as vacuum microgrippers which utilize the suction pressure to hold microparts. Fourth, it largely depends on the capabilities of the work-cells or assembly station.

Moreover, successful, fast and reliable assembly is not limited by but depends on simple interface of joining mechanisms and optimal path planning. In our microfabrication Lab, a 3-D microassembly system [3.2] facilitates multiple constructions of 3D components.

3.2 Microassembly System

The robotic workstation used for the microassembly process is developed in our research institute, ARRI. It is a 3-D microassembly station consisting of 19 DOFs (Degrees of Freedom) with stereo microscope vision. A schematic drawing of the

system is illustrated in Fig. 3.1. The system includes: one stage, two manipulators and a vision system made up of two CCD cameras and two monitors.

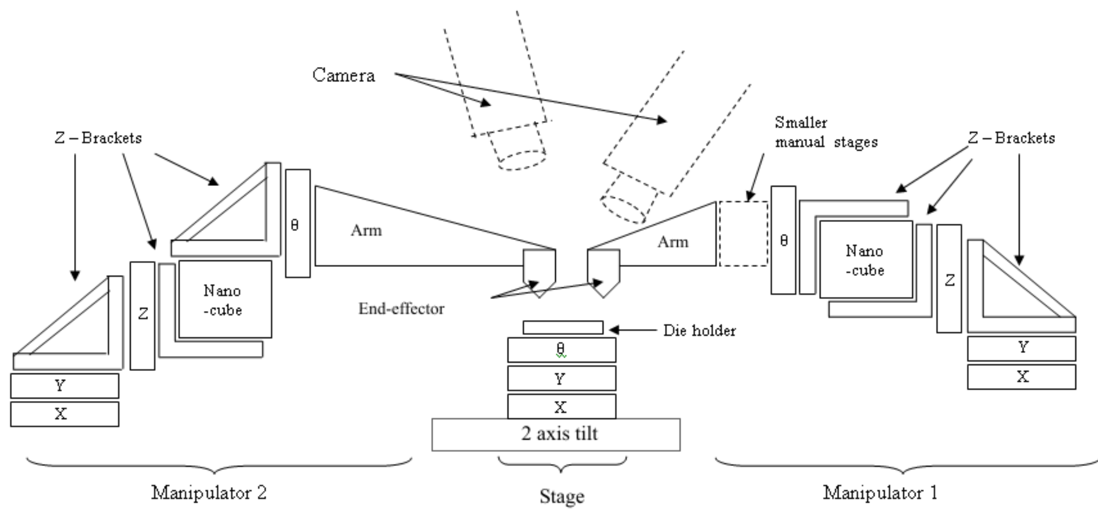

Figure 3.1 A schematic drawing of the 3-D micro assembly system.

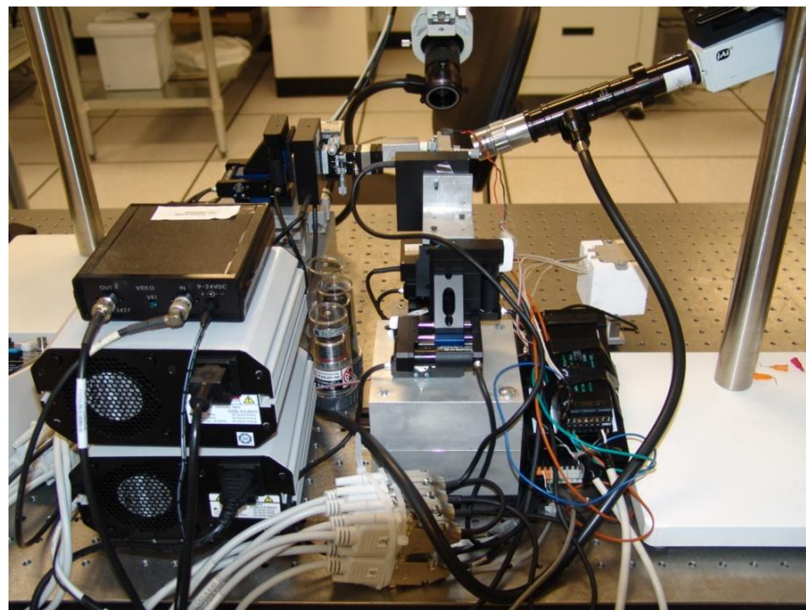

Figure 3.2 A photo of the system setup.

The central stage consists of 5 DOFs with high precision including XYθ and 2 axis tilt. The MEMS chip will be mounted on top of the stage. Each of the two robotic manipulators consists of 7 DOFs. A PI nanocube (1 nm resolution) is mounted between the XYZ linear stage (0.05 μm resolution) and the rotation stage, which enables the resolution of movements in nanometer scale. The capability of rotation is very critical to direct assembly which can orient the microcomponent to the targeting position with specific angle. An end-effecter is mounted at the front end of the robotic arm to manipulate the microcomponents. Adaptor blocks have been designed to provide either vacuum air or electrical signal to the end-effecter. As a result, both of the passive and active microgripper can be used in this system. Here "passive" refers to it does not require actuation. It can be vacuum gripper or micro jammers, etc. An assembly script is written in LabVIEW for automated assembly of MEMS structures. It also provides easy access to the motorized DOFs and controls the station and manipulators.

3.3 Overview of Assembly Process

A MEMS chip will be placed on top of the central stage and fixed by double side tape. An appropriate end-effecter is chosen and mounted on the robotic arm according to the interface feature of the micropart to be assembled. After locating the micropart through the vision system, the manipulator will come down to the micropart (Part1) and pick it up. Part1 will be raised up and rotated for 90˚ then carried to another location after a series of translation of movement. When Part1 is aligned to the second microcomponent (socket) on the substrate, it will be lowered and inserted into the socket. A mechanical connection is then formed between the two microcomponents

which will keep Part1 standing perpendicularly on the substrate. Finally, the manipulator will be released from Part1 without damaging the mechanical connection and will be traveled back to its original position.

In order to successfully complete the assembly process, optimized compliance design is very critical. An active joining mechanism is developed to assemble the microparts. The design and implementation of this active lock will be presented in Chapter 4.

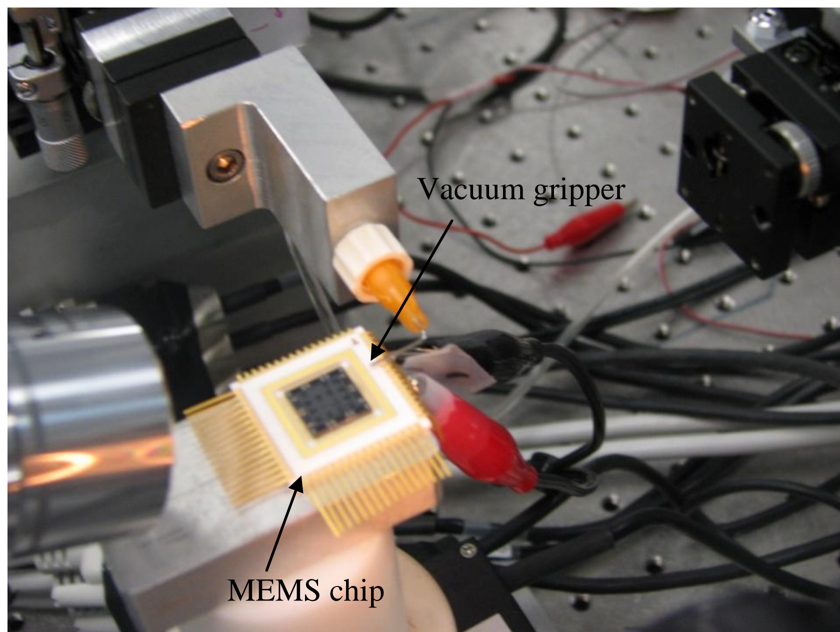

Figure 3.3 A photo of using a vacuum gripper to manipulate microparts.

CHAPTER 4

ACTIVE JOINING MECHANISM

The purpose of this research is to develop a general joining mechanism that can be used to provide a secure and reliable mechanical connection between microparts and substrate. The word "general" refers to that it can be used in various applications. A novel active joining mechanism is proposed and demonstrated in section 4.1. Two different design architectures and their working mechanisms are presented. The module features of the microparts are discussed in section 4.2. As mentioned previously, this joining mechanism can be used in various applications. The module features here are mostly focused on the common features on the microparts which should be suitable for this approach. The fabrication process is described in section 4.3. Finally, the characterization and assembly are reported in sections 4.5 and 4.6 respectively.

4.1 Methodology

The active lock consists of a compliant actuator and a socket. One or two actuators are utilized to squeeze microparts inside of an enclosure opening of a socket. This socket opening is initially narrower than the thickness of the assembled micropart when an actuator is at "CLOSE" state. In order to insert a micropart into the socket, the actuator(s) are activated in order to increase the opening of a socket. The insertion process provides an advantage in avoiding interaction forces during assembly because

the opening of a socket is wider than the thickness of an assembled part. After the actuation is deactivated, the actuators squeeze the inserted parts as the initial opening of the socket is narrower than the thickness of the inserted micropart. The reaction force generated by the compliance of actuators will securely lock the inserted micropart into the substrate.

4.1.1. Choosing Actuators

The compliant actuator should be designed to provide both large deflection and large static force. The first requirement helps open the socket widely so that the allowable tolerance to assemble the micropart is increased. It is also beneficial for the precision of alignment and potentially helps to enhance the speed of assembly. The second requirement corresponds to secured holding force that is resulted from the compliance of an actuator. This enables forming a substantially mechanical connection between the micropart and the substrate or sub-assembly.

Three well-known MEMS actuators are initially considered: electrostatic comb-drive actuators [4.1], pseudo-bimorph actuators [4.2], and chevron beam actuators [4.3, 4.4]. The electrostatic comb-drive actuator operates at a bias voltage around 40-100 V and offers about 0.0059 nN/volt^2 drive force per comb-finger height (μm) [4.5]. A larger force can be generated by arranging multiple comb-fingers in an array but it may take up a large space. The bimorph actuator generates force in the 5-10 μN range [4.6], but the locus of motion is an arc, which is not suitable for the active lock operation. The chevron beam actuator operates by leveraging the deformations produced by localized thermal stress with a lower bias voltage. The consequential deformation is linear and its

force is in the millinewton range [4.6, 4.7], which is suitable to the active joining mechanism.

4.1.2. Overview of Assembly

In our approach, the microparts and active lock are both fabricated on a 4" SOI wafer and patterned by DRIE (Deep Reactive Ion Etching) process. A brief overview of the assembly is described as the following: the micropart is connected with a tether initially in plane. After breaking the tether, the micropart is picked up and oriented 90° by the end-effecter mounted on the assembly station. Then the active lock is turned on and the part is inserted into the socket. Finally the active lock is turned off and the end-effecter is released from the part. According to the active joining mechanism, there is no insertion force required during assembly. For the end-effecter, the only requirement is providing a grasping force to pick up the part and release the part without destroy the assembly. It also needs to be compatible in scale with the micropart. With the considerations above, we choose a vacuum gripper with pre-defined angle of 90°. The diameter at the vacuum tip is around 400 μm.

4.2 Design Architecture

4.2.1. Active Lock Concept

A chevron actuator based on electro-thermo-elastic deformation is essentially a desired concept for providing a tunable socket opening and high compliance force per unit area. This is because the chevron could be arranged to have an array of packed beams linked together with a movable structure. The current passing through the beams generates symmetrical joule heating in the beams. The symmetrical structure and

temperature distribution allow the chevron apex to linearly translate forward. Since chevron actuator has been extensively studied in [4.6, 4.7], here we will only focus on incorporating it into the active sockets.

Two different designs are proposed for this active lock mechanism: single chevron model (SCM) and double chevron model (DCM). In both designs as shown in Fig. 4.1 (a) and (b), the nominal opening of the socket d_1, is less than the thickness of the assembled micropart d_2. In order to achieve zero insertion force during assembly, the total opening of the socket d_3 should be larger than d_2 and greater tolerance ε ($d_3 > (d_2 + \varepsilon)$). After the socket is close, the actuator squeezes the inserted part with a deflection ($d_1 - d_2$). The interaction force generated by the compliance of the stretched chevron will lock the inserted micropart into the substrate.

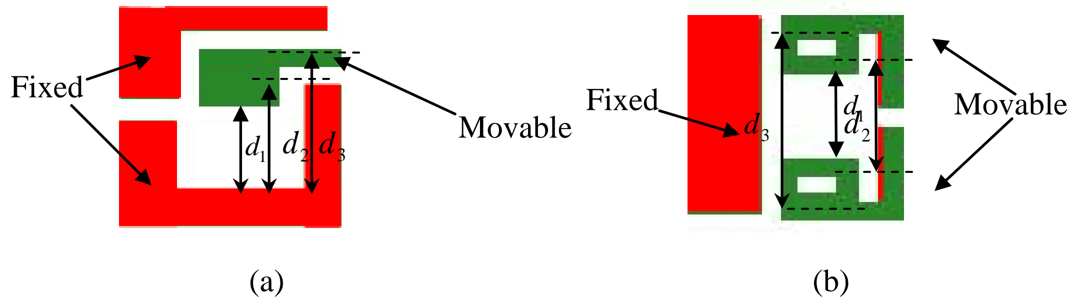

Figure 4.1 The design concept of active joining mechanism is illustrated by (a) single chevron model and (b) double chevron model respectively.

When an assembled part is damaged, the active lock can "OPEN" and let it go. Same assembly process can be repeated to replace the part. To fix the micropart in the socket, a thin layer of solder metal can be deposited on the inserted finger and the sidewall of the socket. The attachment occurs during solder melting which also forms

the electrical interconnect between the assembled part and the substrate. The soldering issues will be discussed in section 4.6.

4.2.1.1. Single Chevron Model (SCM)

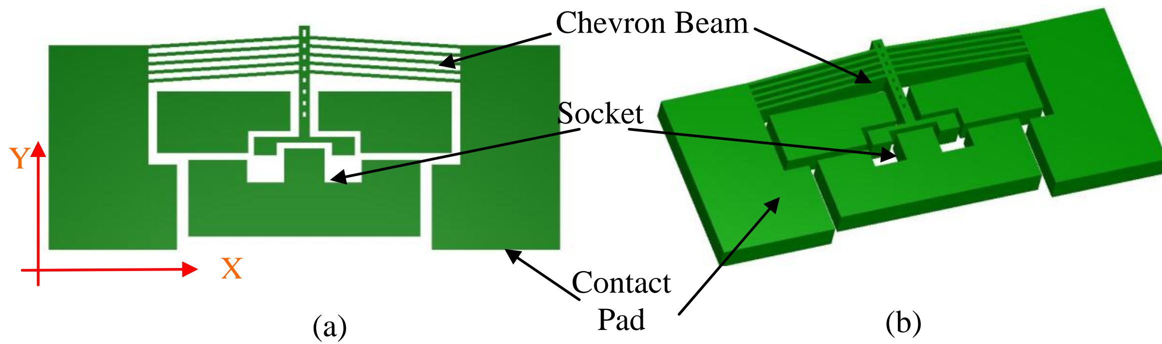

Figure 4.2 The (a) top view and (b) 3-D view of the single chevron model.

A schematic drawing of the single actuator model is illustrated in Fig. 4.1. The active lock consists of an actuator and a socket. Three sides of the sockets are fixed on the substrate and only one side is controlled by an electro-thermal actuator. The electro-thermal actuator described here resembles a chevron where an array of buckle-beams are packed close together and link two common anchored arms with a movable structure. By applying voltages on the contact pads, the actuator deforms along the *y*-direction, which opens the socket. The mechanical spring force restores the actuators back to the original location after releasing the biasing voltage and closes the socket.

4.2.1.2. Double Chevron Model (DCM)

A schematic drawing is illustrated in Fig. 4.3. It consists of two electrical contact pads, a pair of chevron beam actuators, and a gap (socket) separated by two actuators (as shown in Fig. 4.3 (b)). Comparing with the single chevron model, the

Double chevron model provides more clearance for inserting microparts due to the larger opening on both sides of the sockets.

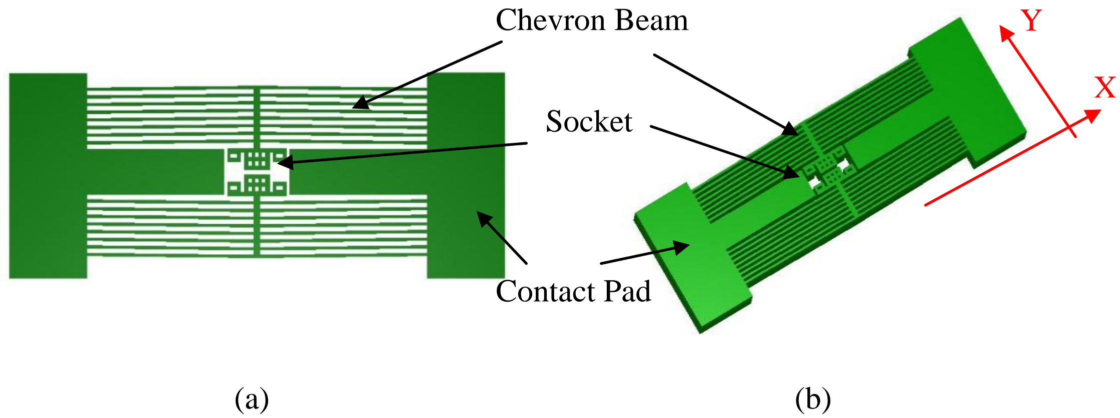

Figure 4.3 The (a) top view and (b) 3-D view of the double chevron model.

4.2.2. Actuator Design

4.2.2.1. Deflection

In order to perform assembly successfully, the chevron beam actuator has been carefully designed. A chevron beam actuator is one of the electro-thermal actuators, which rely on the joule heating and its resulting small mechanical expansion of a conductor when a current passes through it. The actuator design is based on an in-plane buckle-beam actuator, as shown in Fig. 4.4. The beam is normally designed with an inclined angle α so that buckling initiates a certain direction, i.e. y-axis. The displacement of the apex of actuators is a function of the slope and the dimensions of beams.

The actuator displacement d is given [4.8] by

$$d = [l^2 + 2(l)l' - l\cos(\alpha)^2]^{1/2} - l\sin(\alpha) \qquad (4.1)$$

where l is the single beam length, l' is the elongation of the beam due to thermal expansion, and α is the pre-bend angle of the beam.

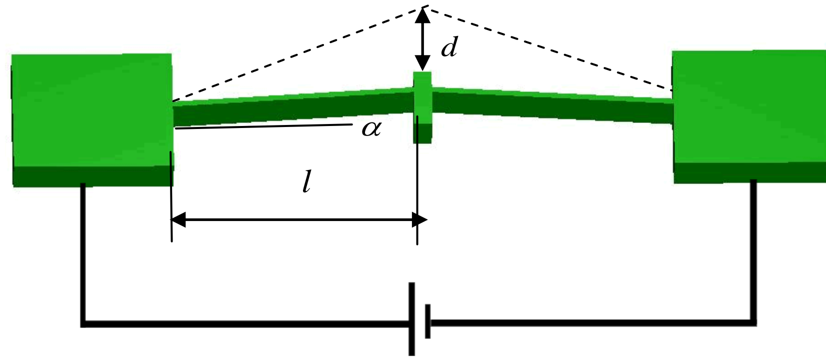

Figure 4.4 Single buckle-beam actuator.

The applied voltage causes joule heating and expansion between the two fixed anchors, buckling the beam at the midpoint. Finite element analysis (FEA) was used to calculate the displacement of the actuators by varying the applied voltage from 1 to 12 V. The dimensions of the chevron beam actuator are listed in Table 4.1. The material properties of single crystal silicon that used in FEA are shown in Table 4.2.

Table 4.1 The design parameters of single chevron model and double chevron model.

Actuator Design	Single Chevron Model	Double Chevron Model
Beam Length (μm)	530	1005
Beam Width (μm)	12	15
Beam Thickness (μm)	100	100
Bent Angle (^{o})	3.5	0.5

Table 4.2 The parameters of single crystal silicon used in FEA.

Layer Parameters	Device Layer Silicon
Density, ρ_d (Kg/m)	2330
Thermal Conductivity, k (Wm^{-1} ℃$^{-1}$)	100
Thermal Expansion, α ($10^{-6} \times$ ℃$^{-1}$)	3.1
Thermal Capacity, C_p (JKg^{-1} ℃$^{-1}$)	787
Temperature Coefficient, ξ ($10^{-3} \times$ ℃$^{-1}$)	1.25
Electrical Resistivity, ρ_0 ($\Omega.m$)	1x10^{-4}
Young's Modulus, E (GPa)	169
Poison Ratio, v	0.22
Yield Stress (MPa)	5000-9000
Melting Point (℃)	1414

4.2.2.2. Force

The reaction force, f_{max}, is proportional to the number of buckle-beams, actuator layer thickness and pre-bend angle. The analytical formulation of reaction force is given by [4.9]:

$$f_{max} = d_{max} K_y = d_{max} \times \frac{4\sin^2(\theta')AE}{L} N \tag{4.2}$$

where $$\theta' = a\tan\left(\frac{d_0 + d_{max}}{L/2}\right) \tag{4.3}$$

A is the cross sectional area.

L is the length between two pads.

E is the device layer modules of elasticity.

K_y is the spring constant.

N is the total number of V shape bean in one side.

d_0 is the beam height from horizontal line and cause by θ_0.

d_{max} is the deflection of the beam after assembly.

θ' is the effective bending angle and may differ from the actual angle as a result of apex displacement.

Table 4.3 The design parameters for the reaction force after assembly.

	A(m²)	L(m)	N	θ(°)	F(mN)
Double Chevron	$15\times10^{-6}\times100\times10^{-6}$	2012×10^{-6}	8	0.5°	3.9
Single Chevron	$12\times10^{-6}\times100\times10^{-6}$	1060×10^{-6}	5	3.5°	92.76

The sockets open 18 μm with the applied voltage at 12 V (Fig. 4.6(a)) in SCM. The maximum stress at 12 V is 236 MPa which is below the yield stress of single crystal silicon. As a result, the micropart is locked in the substrate by the deformation of chevron beams with the reaction force of 92 mN after assembly. In DCM, the total opening of the socket is 68 μm (Fig. 4.6 (b)) and the maximum stress is 459 MPa at 12 V. After assembly, a 5 μm deformation of each actuator generates 3.9-mN reaction force that we estimated by FEA simulation. It's difficult to achieve both the large deflection and large static force at the same time due to the design tradeoffs.

Accordingly, SCM is designed to provide larger static force and DCM is for larger deflection.

(a) (b)

Figure 4.5 The schematic drawings of the socket design in (a) single chevron model and (b) double chevron model.

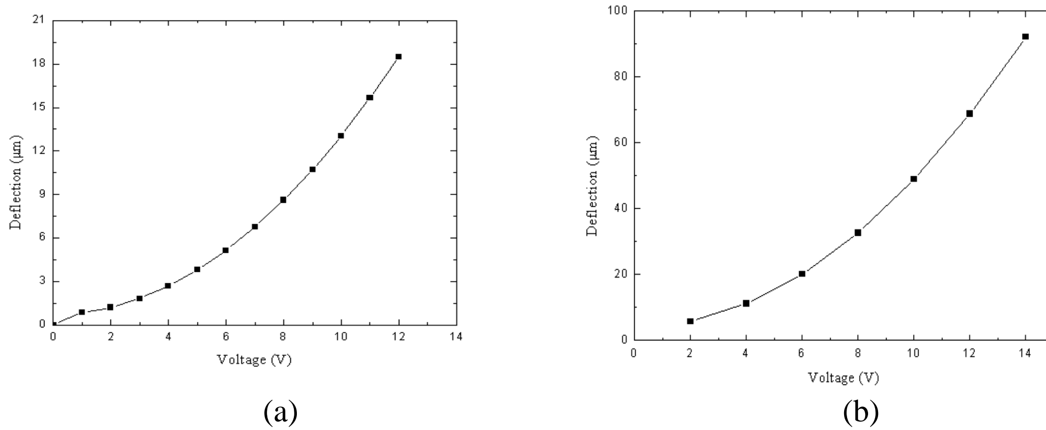

(a) (b)

Figure 4.6 FEA simulations of the opening of the sockets as a function of the applied voltage of (a) single chevron model and (b) double chevron model.

4.2.3. Micropart Design

Three main module features are considered for the design of microparts: (1) the interface between the micropart and the active lock, (2) the interface between the micropart and the end-effecter during assembly, and (3) tether which restrains the micropart on the substrate before assembly.

Due to the working mechanism of the active lock, the socket can open and close along *y*-direction. For the socket fabricated using the SOI wafers, the minimum length in the *y*-direction is determined by the maximum aspect ratio of the DRIE process. The width of the socket in *x*-direction is designed larger than the width of the micropart plus the assembly tolerance. The micropart consists of two fingers that will be inserted into the socket, a pair of pick-up holes for a microgripper to grasp, and two tethers to connect the micropart with the substrate after release. The *x*-*y* dimensions of the fingers are 100 μm x 100 μm, and the thickness in the *z*-direction is 100 μm. Two stoppers are added on the each side of the micropart indicating a complete insertion of the fingers.

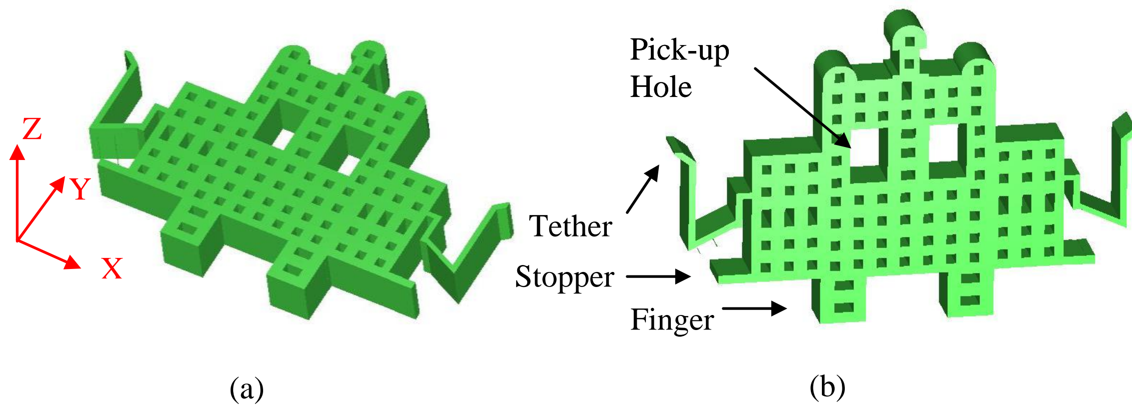

Figure 4.7 The schematic drawings of the micropart (a) before assembly and (b) after assembly.

4.3 Fabrication Processes

The fabrication process starts with a 4” SOI wafer (thickness of the handle layer = 400 μm, thickness of the buried oxide = 2 μm, thickness of the device layer = 100 μm, p-type, single crystal silicon, sheet resistance = 0.01-0.02 Ω -cm) and the process sequence is illustrated in Fig. 4.8. The fabrication process includes two main parts.

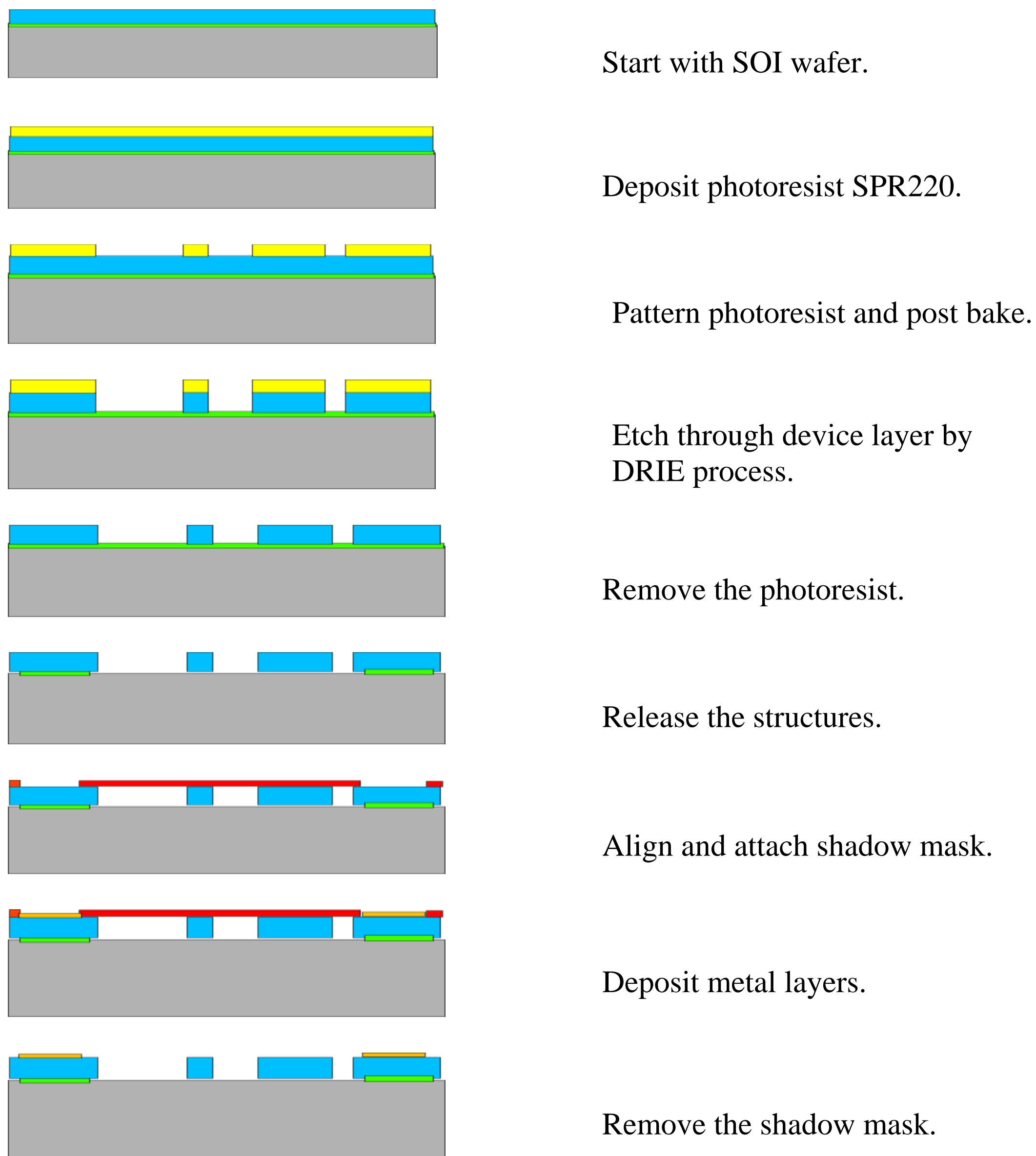

Figure 4.8 The cross-sectional view of the SOI wafer during fabrication.

First, pattern the device layer. A 3 μm thick photoresist, SPR220, is spin coated on top of the wafer, then patterned. The photoresist is used as the mask during the following DRIE (Deep Reactive Ion Etching) process to etch through the device layer. A 30 minute baking in a 110 ℃ oven was performed to further harden the photoresist in

order to prevent from the undercut etch by the plasma during DRIE. The device layer is etched by 100 μm with a STS Etcher using the DRIE (Bosch) process which produced a smooth side wall. The roughness of sidewall is about 200 nm.

Afterward, the remaining photoresist is removed by a Gasonics plasma asher. 49% concentrated HF (hydrofluoride acid) is used to undercut the oxide about 30 μm. Finally, the wafer is dried in an Automegasamdri-915B Critical Point Drying (CPD) system.

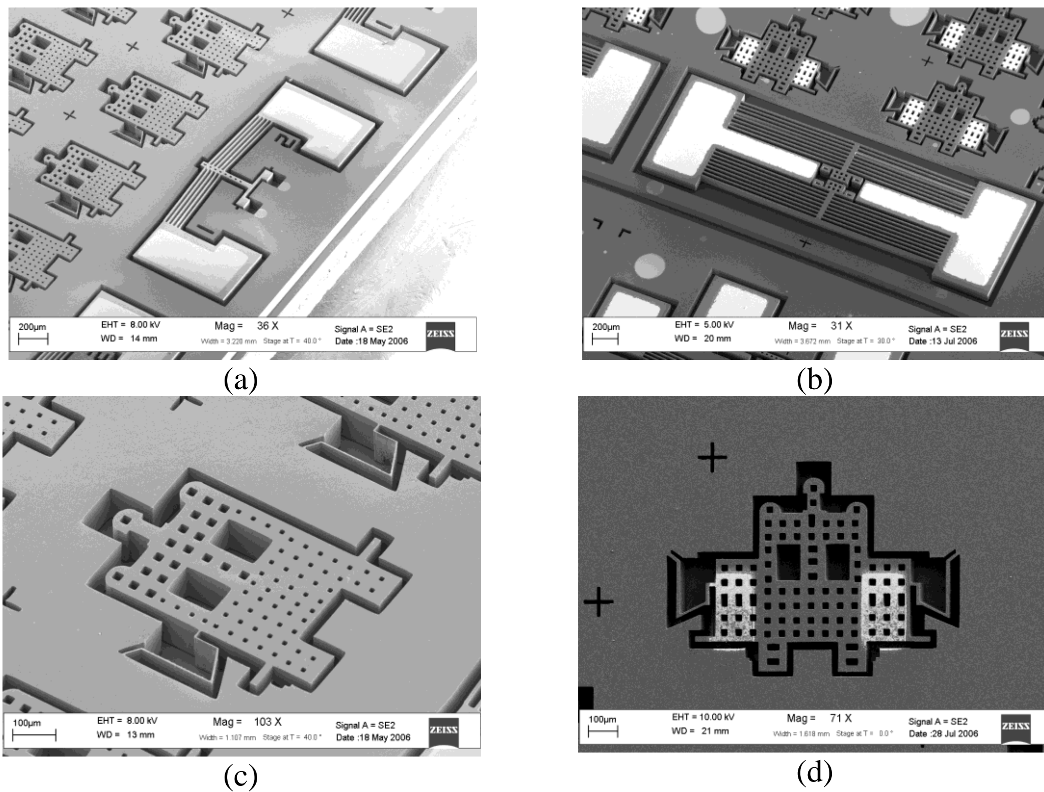

Figure 4.9 The SEM photos of the fabricated devices. (a) A single chevron active lock. (b) A double chevron active lock. (c) A micropart. (d) A micropart with metal.

Second, deposit metal. A shadow mask, which is made by etching though a 375 μm silicon wafer, is aligned to the processed SOI wafer and subsequently temporarily

bonded by a Kapton tape at the edge. This polyimide tape has an operating temperature up to 260 ℃ and can be removed cleanly without an adhesive residue after exposure to heat. The metal layers, 100 Å of chromium and 1000 Å of gold, are evaporated to form the metal pads on the SOI wafer. Finally, the shadow mask is removed and the SOI wafer was diced into 1 cm x 1 cm die by laser.

4.4 Assembly Procedures

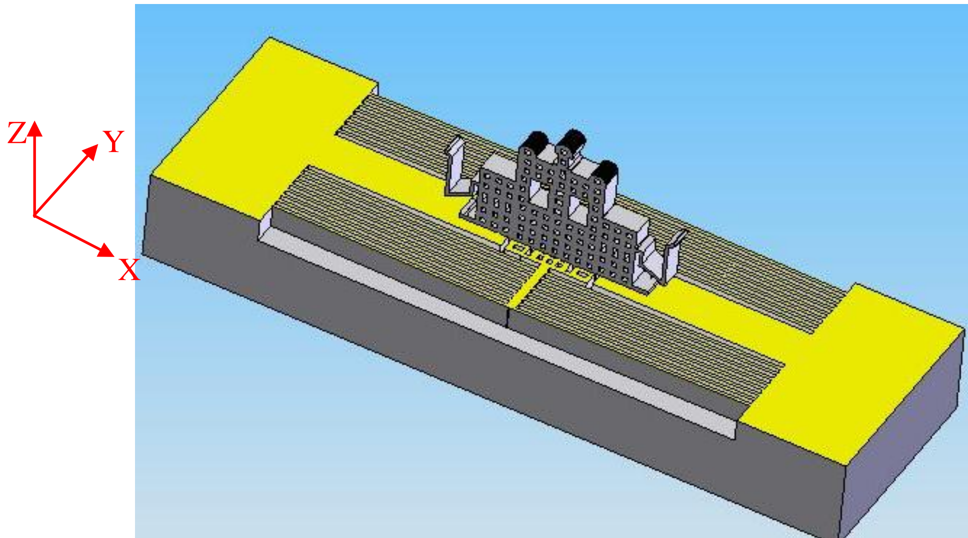

Figure 4.10 A schematic drawing of the assembled micropart using the active lock.

As shown in Fig. 4.11, the pictures are taken during the assembly of a micropart using DCM. A vacuum gripper is used as the end-effecter to pick up and place the micropart. The diameter of the vacuum tip is about 400 μm.

Before assembly, all the microparts are constrained in the device layer by tethers. In order to pick up the part by the end-effecter, the tether has to be broken first. It can be done either by a probe or a microgripper.

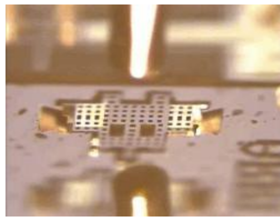
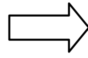
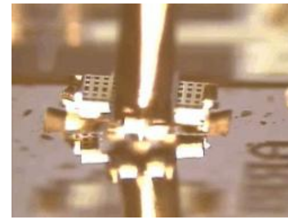

Pick the micropart by the vacuum tip.

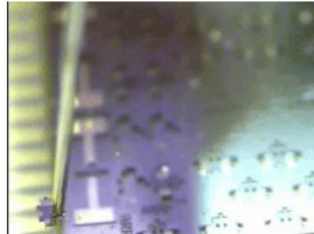
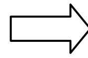
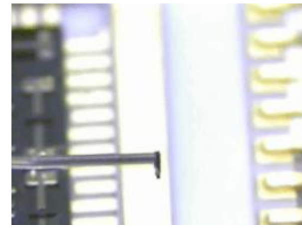

Rotate the micropart and align it onto the sockets.

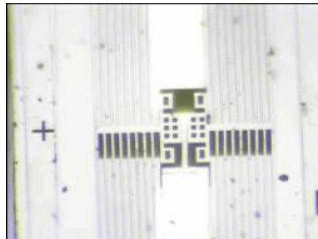
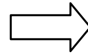
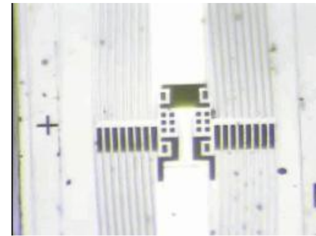

Open a socket for zero-force insertion.

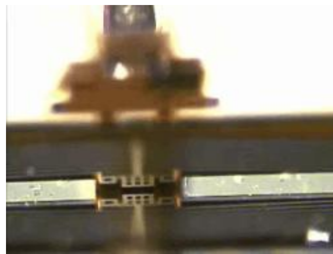
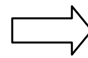
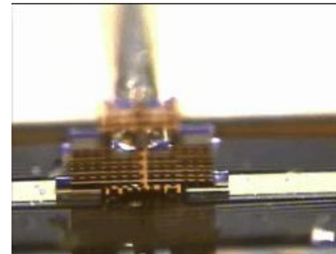

Insert the micropart into the socket.

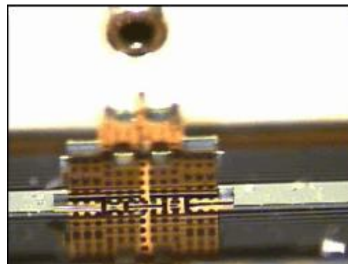
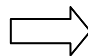
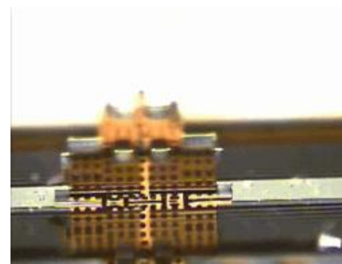

Release the socket and remove the vacuum needle.

Figure 4.11 The assembly process.

As shown in Fig. 4.11, the assembly procedures are: (1) tether breaking and picking up of a micropart, (2) a series of translation and rotation of a mating micropart to align it onto the socket, (3) opening of a socket area for zero-force insertion, (4) insertion of a micropart into the socket, and (5) deactivation and releasing of locking fingers. As a result, the micropart was held vertically to the substrate and locked by the compliance of the chevron beams.

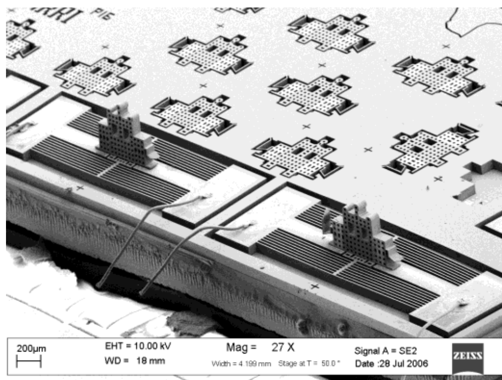

(a)

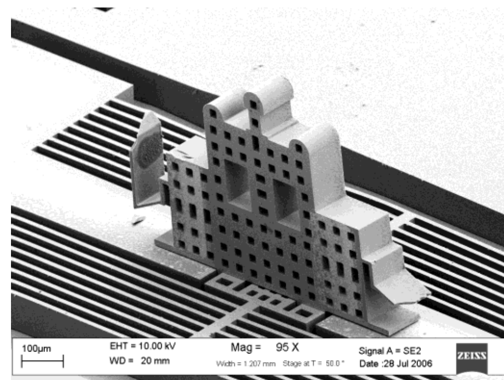

(b)

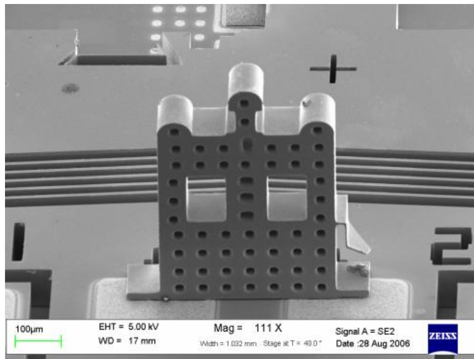

(c)

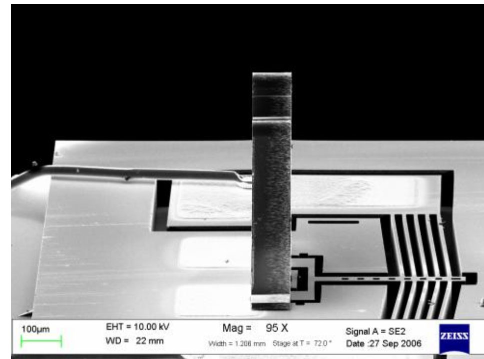

(d)

Figure 4.12 The SEM photos of the assembled microparts. (a) Two microparts are assembled in a row. (b) One micropart is assembled with the double chevron model. (c) One micropart is assembled with single chevron model. (d) The side view of one assembled micropart.

Figure 4.12 shows SEM photos of assembled microparts. Two assembled parts in a row are shown in Fig. 4.12 (a). Six microparts have been assembled using DCM and five microparts using SCM with a 100% successful rate. The fingers of the microparts are fully inserted into the socket and the microparts stands perpendicularly to the substrate.

The assembly by using single chevron model (SCM) is similar to the assembly process of double chevron model (DCM).

4.5 Characterization

4.5.1. Before Assembly: Socket Opening

The MEMS die with the active lock and microparts was bonded to a Leaded Chip Carrier (Flat Pack) by epoxy and its electrical pads are wire bonded. The performance of the active lock is characterized using a Wyko DMEMS NT1100 optical profiler.

The deflection of the chevron beam actuator is measured by applying an excitation voltage across the two metal coated pads. The deflection as a function of biasing voltages is shown in Fig. 4.13 which determines the minimum input voltage that guarantees successful assembly with a certain tolerance budget.

The measured deflection of the actuator in SCM is 12.6 μm and 22 μm for one side in DCM with the supplied voltage of 24 V. The total opening of the socket in DCM is doubled as the pair of chevron actuators is symmetrical. So the total opening is 44 μm in DCM. Compared with the simulated result, both of the two models consume more

power in the experiment than the simulation. The main reason is due to the increased resistance which is caused by contact resistance from wire bonding.

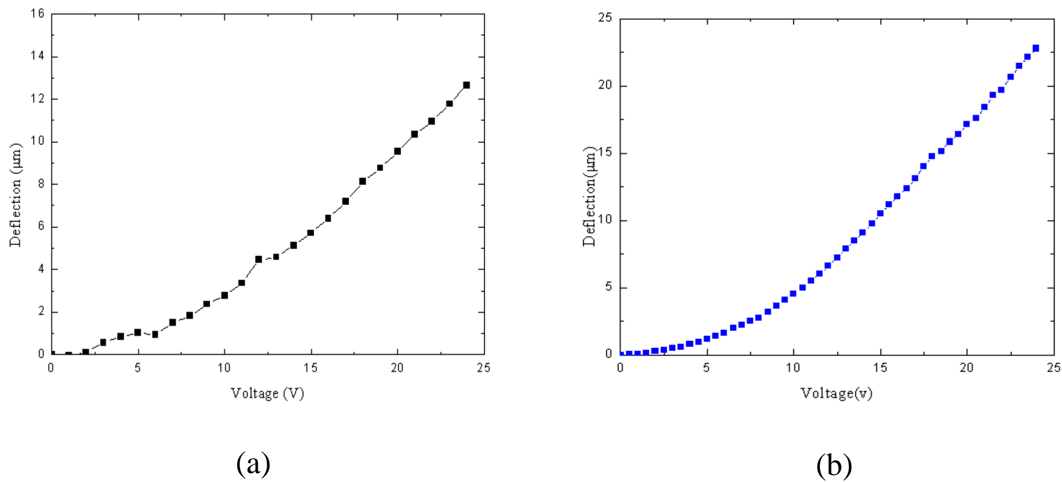

Figure 4.13 The plots of the deflection of the chevron actuator as a function of the applied voltage for (a) single chevron model and (b) double chevron model.

4.5.2. *After Assembly: Force Characterization*

After inserting the microparts, the pull out force, which disengages the assembled microparts from the sockets, is characterized by the following experiments.

4.5.2.3. Experimental Setup

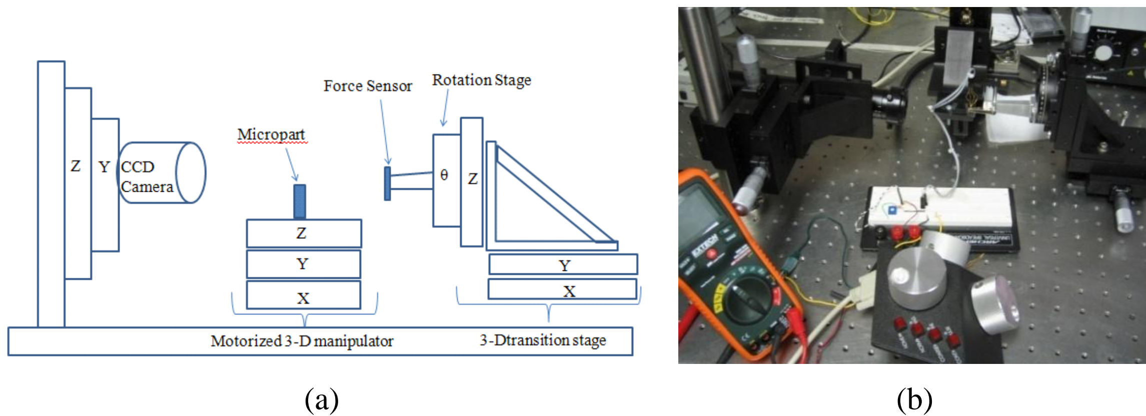

Figure 4.14 (a) The block diagram and (b) a photo of the force measurement setup.

A block diagram of the set up for force characterization is illustrated in Fig. 4.14 (a). An AE-801 force sensor is mounted on a rotation stage with an XYZ transition stage which is used to measure the reaction force on the micropart. The MEMS chip that contains several assembled microparts is attached to a MP-285 motorized 3-D manipulator. A CCD camera is mounted on a 2-D stage to monitor the motions of the force sensor and assembled micropart.

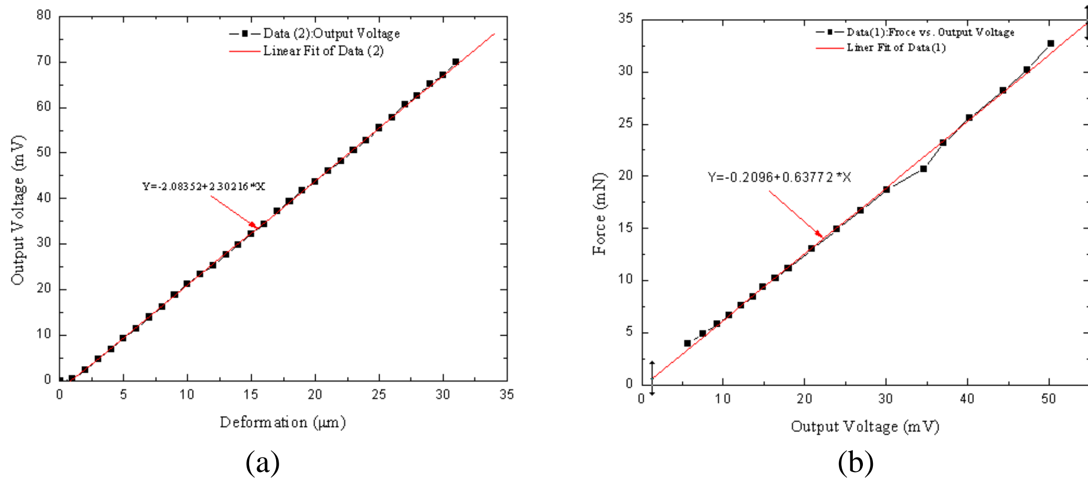

Figure 4.15 Characterizes the force sensor. (a) The deflection as a function of voltage. (b) The force as a function of output voltage.

The force sensor is first balanced with a wheatstone bridge circuit [4.10]. Then it is calibrated experimentally with two tests. First, a controlled transitional displacement is imposed on the tip of the force sensor by using a rigid edge carried by the motorized manipulator. The relation between the output voltage signal and the displacement is plotted in Fig. 4.15 (a). Second, an external force is applied on the tip of the force sensor and increased gradually by adding a series of measured weights. The voltage output is recorded at each point of the external force as shown in Fig. 4.15 (b).

Both of the Figures (Fig. 4.15 (a) and (b)) demonstrate good linearity in force sensing. The reaction force at the tip of the force sensor can be correlated with the output voltage signal in later force test.

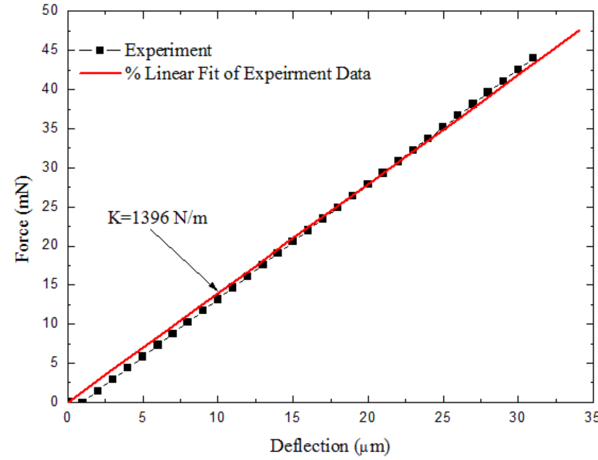

Figure 4.16 The plot of experimental spring constant at the tip of the force sensor.

The slope of linear fit of the experimental spring constant is 1396 N/m. The dimension of the cantilever bean is 5 mm (*L*) x 950 µm (*w*) x 150 µm (*t*). Its Young's modulus is 1.6 x 10^5 N/mm^2 and the spring constant *k* is 1026 N/m. This calibrated sensor will be used to push the assembled micropart out of the socket.

$$k = \frac{Ew}{4}\left(\frac{t}{l}\right)^3 \tag{4.3}$$

where *E* is the modulus of elasticity, *w* is the width, *l* is the length and *t* is the thickness of the cantilever beam.

4.5.2.4. Measured Results

As shown in Fig. 4.17, the force sensor is fixed on the rotation stage. The MEMS chip is attached on the motorized manipulator and will move together against the force sensor. When the assembled micropart hits the force sensor during traveling,

the tendency to move against the force sensor results in a deflection at the tip of the force sensor which will generate an output voltage signal. The manipulator moves with a 1 μm step resolution and the output voltage is recorded from where the micropart gets into contact with the force sensor. A direct pullout force and a torque are applied on the micropart as shown in Fig. 4.17. The reaction force at the tip of the force sensor versus the output voltage signal is illustrated in Fig. 4.16.

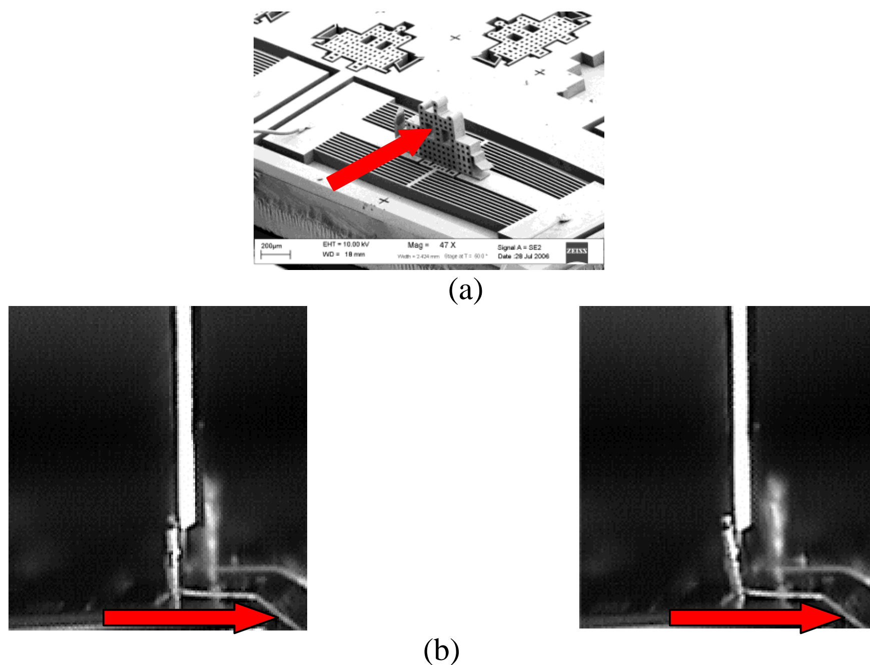

Figure 4.17 Photos of the assembled parts with double chevron model being pushed by the force sensor. (a) The direction and location of the applied force by the force sensor. (b) Cross-sectional view of the force sensor pushing one assembled micropart.

The measured force as a function of the moving distance of the motorized manipulator which carries the assembled parts is shown in Fig. 4.18. For Double chevron model, two chevron actuators are symmetrical so the forces generated from the bent beams cancel out each other and align the part in the center of the socket. When

being pushed by the force sensor, the inserted fingers slip inside the socket until they come out of the sockets since the actuators are flexible on both sides. Until the part comes out of the socket, the active lock remains good without any damage. The maximum forces exhibited are 6.29 mN and 6.67 mN from two assembled parts respectively. Further experiment is performed by releasing the pushing force through moving the assembled part gradually away from the force sensor in the middle of the process before the part comes out from the socket. The elasticity of the active lock makes the part come back to its original position at the center of the socket.

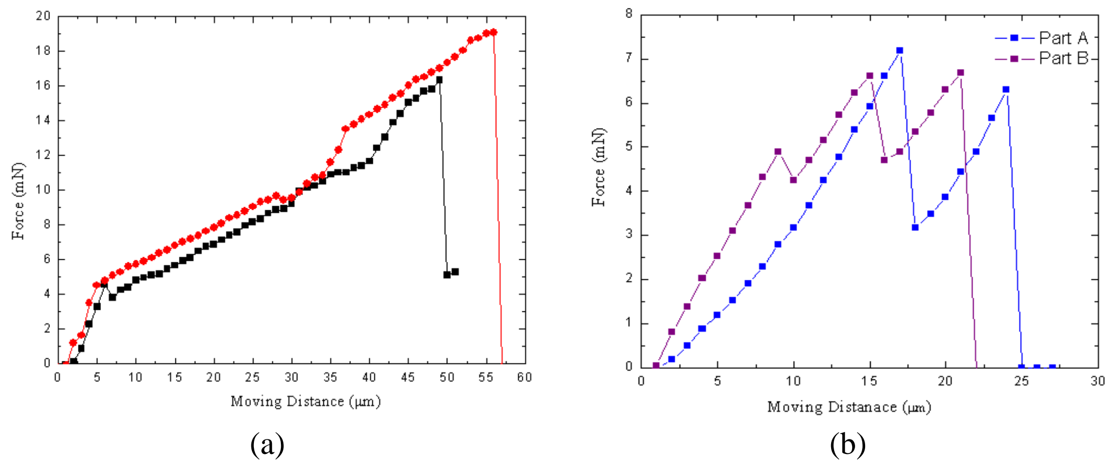

Figure 4.18 The plot of the force applied on the assembled microparts as a function of moving distance in (a) single chevron model and (b) double chevron model.

For single chevron model, the holding force pushes the inserted finger against one fixed edge of the socket. After assembly, the movable arm connected to chevron actuator moves within a 20 μm gap between the assembled part and a fixed edge of the socket. When pushing the micropart, it slips and then stuck in the socket when the movable arm hits the socket. So the force is recorded at that point when the assembled

start to leave its original position. The forces are measured as 16.3 mN and 19 mN from two assembled microparts.

4.6 Soldering

4.6.1. Process Requirements

Soldering has been widely used in flip-chip bonding because it can provide not only strong bonding strength but also electrical interconnection. Two critical process parameters for a reliable soldering are temperature and pressure. The first condition can be achieved by global heating or local laser welding. The second one is normally provided by external load and applied on the whole wafer/chip. Applying external load on the substrate that contains 3-D assembled microstructures is extremely difficult since it can easily fracture the assembled MEMS structures. If the mechanical interconnection can provide the required pressure to the metal contact area, soldering may occur under optimized conditions. In the active lock design, the deformation of the actuator provides a holding force to squeeze the inserted part. When design properly, the pressure at the contact area can be served as an external load to facilitate the reflow of solder.

One solder composition (80Au/20Sn) is experimented as interconnect metal which has been investigated using fluxless soldering process for hermetic sealing [4.10-4.14]. A thin layer of solder metal (Gold/Tin) is deposited by sputtering from a solder alloy target using the same metal pattern in section 4.3. The previous deposited Au and Cr layers serve as the base metal for the solder. The metal layers including base and solder metal are coated on the top surface of fingers of the microparts and the sidewall

of the sockets. After insertion, the inserted fingers and sockets have a metal to metal contact surface as shown in Fig. 4.19.

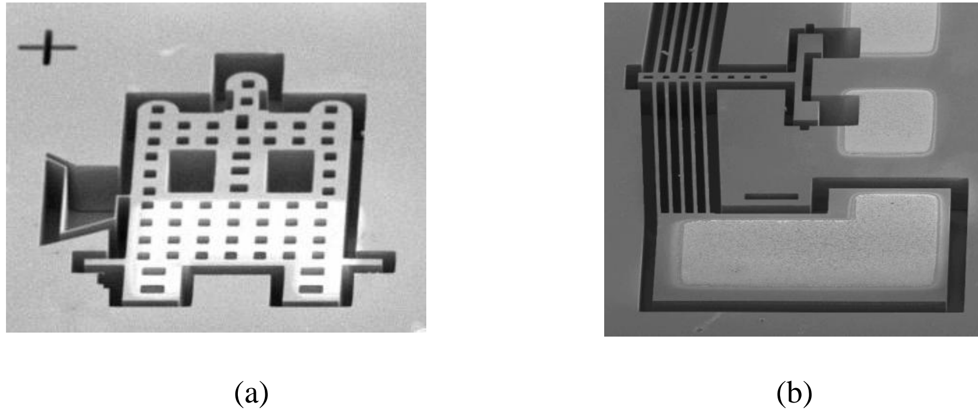

(a) (b)

Figure 4.19 The solder coated (a) micropart and (b) socket.

The bonding temperature and pressure are indentified through a series of experiments by using a Laurier M-9 Flip Chip Aligner Bonder. The solder metal and base metal are deposited on a flat wafer surface. Afterwards, the wafer is diced into 1 cm x 1cm chips and then divided into several pairs which contain the same metal patterns. Experiments are performed to explore the process parameters to form good bonding by using the Flip chip bonder. The results show that bonding occurs at 320 ℃ with applied pressure from 1 to 3 MPa in a vacuum environment.

In the single chevron model, the reaction force resulted from the deflection of the actuator is 92mN and is distributed uniformly on the inserted fingers of the assembled micropart. The dimension of the contact area is 100 μm × 100 μm for each finger. So the pressure at the contact $P = \frac{F}{S}$ is 4.6 MPa. Similarly, the pressure in

double chevron model is found as 0.2 MPa. The pressure in SCM is analytically sufficient for soldering.

4.6.2. Experiments and Primary Results

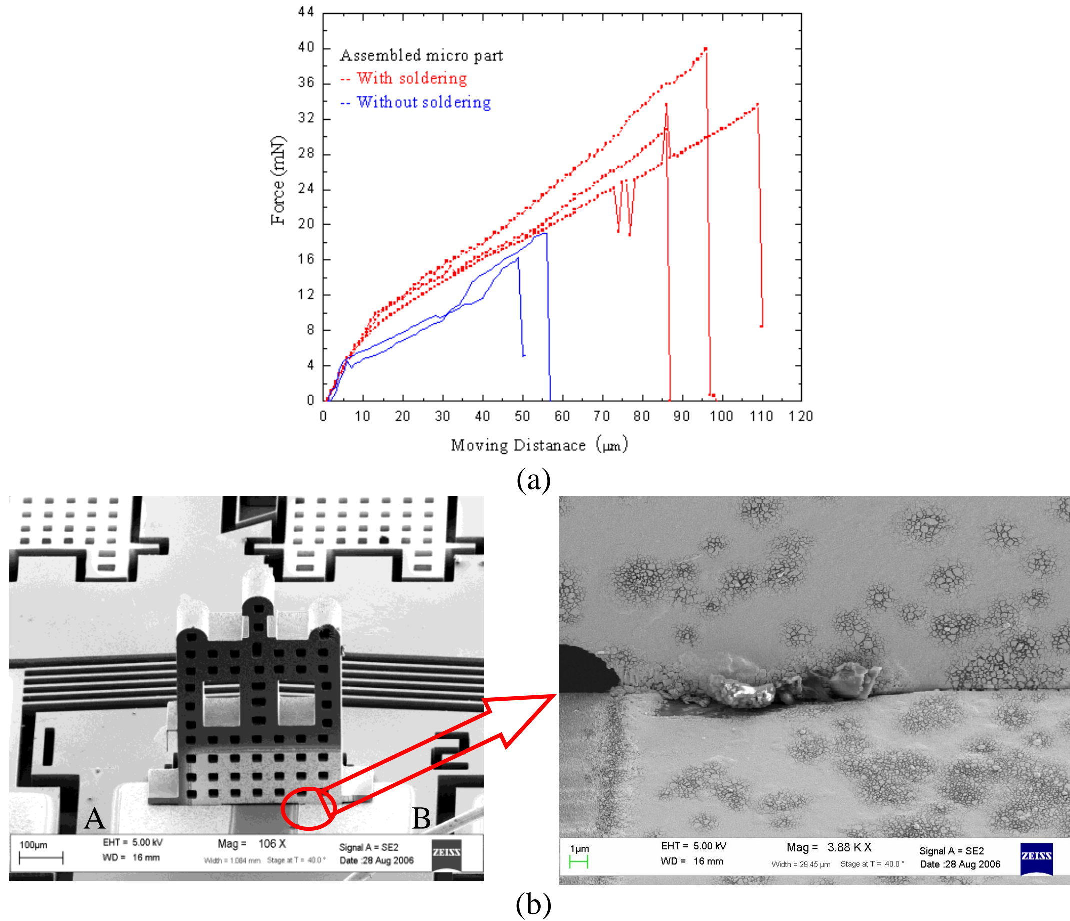

Figure 4.20 The force measurement on the soldered microparts. (a) The plot of the force applied on the assembled microparts as a function of the moving distance of the motorized manipulator with and without heating. (b) SEM photo of an assembled micropart with solder metal depositied on the contact area on the inserted finger and sidewall of the socket.

Bonding experiments of the assembled MEMS chip (SCM) is performed by heating them up to 320 ℃ and kept for 10 minutes in a Blue M oven whose temperature can be well controlled. After cooling down to room temperature, force test to push the

assembled microparts are performed on the same chip tested previously. The purpose is to evaluate the reflow and strength of soldering and how it will affect the stiffness of the mechanical connection.

As shown in Fig. 4.20, the plots in solid line show the force test without soldering and dot line for soldering. Without soldering, the maximum forces demonstrated by two microparts are16.3 mN and 19 mN respectively. After the heating procedure, three assembled microparts are participated in the force test. The largest force exhibited is 39.9 mN and the minimum one is 30.8 mN. The moving distance of the motorized manipulator also shows a big difference in the two experiments. Without soldering, the first break point is observed after the manipulator travels 50 μm and 57 μm. With solder bonding, it is observed at 88 μm, 97 μm, and 130 μm.

The soldering demonstrated improvement of the mechanical stiffness of the sockets. However, the quality of the solder wetting is not repeatable. This may result from the different oxidation level of the solder metal. Because the reflow process is not performed in vacuum or nitrogen environments, the oxygen will dramatically increase the oxidation during heating the solder metal.

Electrical resistance is measured by probing the metal pads A and B on the sockets as shown in Fig. 4.20 (b). The measured data are 9.9 Ω (before soldering) and 9.7 Ω (after soldering) respectively. The measured resistance includes the resistance between the two metal pads and the two contact resistances of the probe with metal pad. The experiments don’t show big differences in the resistance change due to the two sockets are connected through the device layer which is highly conductive. It can be

avoid by separating the sockets a deep trench, which can be etched out during DRIE process.

4.6.3. Summary

In summary, an active joining mechanism for 3-D microassembly is demonstrated. The design concept is illustrated by two models and microcomponents are designed, fabricated and characterized. The module features of the assembled micropart have been presented, which included the interface with the socket, the interface with the end-effecter and the tether feature. Both of the active locks have been successfully demonstrated for constructing 3-D microstructures. The design tradeoffs have been discussed. The active lock shows very good feasibility for forming substantial mechanical interconnection. Solder metal can be deposit on the contact surface of the interconnection and form bonding under inert or controlled conditions. Primary results show that it not only enhances the mechanical stiffness but also potentially forms electrical interconnection simultaneously. Both of them can be used for constructing 3-D structures according to the requirements of different applications. Two applications implemented by this active joining mechanism will be presented in Chapter 5.

CHAPTER 5

APPLICATIONS

5.1 DWDM

DWDM is a key device in optical communications. It works by combining and transmitting multiple signals simultaneously at different wavelengths on the same fiber. In free-space system, it's made up of multiple filters with different passbands. Traditionally, the assembly of these filters is normally performed manually. First, epoxy is applied on the filters followed by adjusting its positions to meet the optical requirements. After the desired spectral shape is achieved, epoxy is cured to fix the filter permanently. The assembly process is costly and very time consuming because of the multiple filters in the system. By utilizing active locking mechanism, the filter assembly can be as simple as dropping the filter into the socket at the desired location. Precisely optical alignment can be achieved by the self-aligned feature of the active lock

5.1.1. Socket Design and Assembly

The multi-layer thin-film filters we used are bought from Barr Associates, Inc [5.1]. The thickness is 1.2 mm±0.1 mm. The other two dimensions are measured between 1.16 mm to 1.18 mm. In order to insert the filters, the socket has to provide appropriate tolerance to compensate the variances in both dimensions, which are 200

µm and 20 µm respectively. Double chevron model is utilized in the socket design due to its large deflection. The socket is designed as 1160 µm x 1450 µm. Accordingly, the fixed side of the socket is 250 µm larger than the nominal dimension of the filter thickness. On the movable side, same design parameters are used as the previous one in section 4.2, which can provide a total opening of 44 µm with an applied voltage of 25 V.

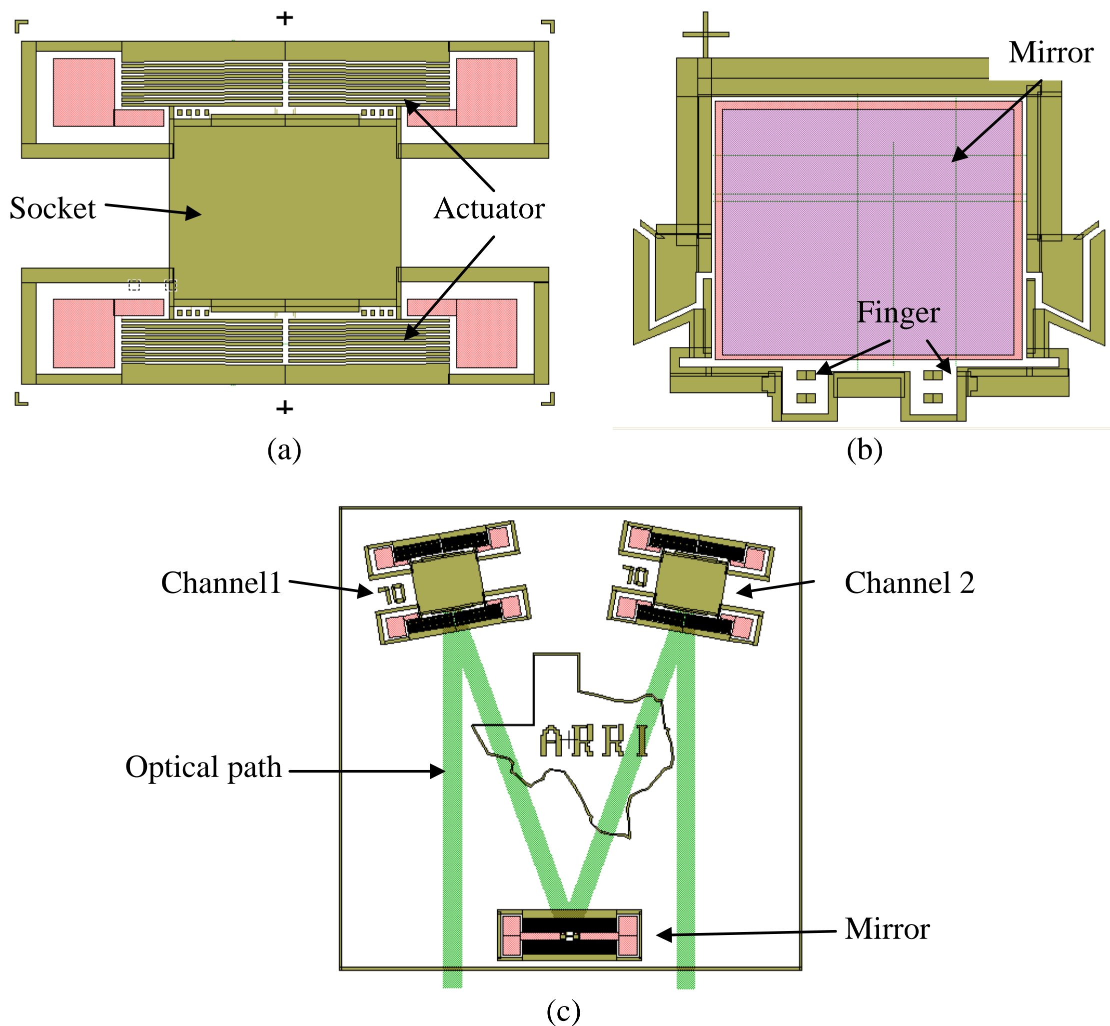

Figure 5.1 The design layouts of the (a) active lock for assembling the filter, (b) micromirror and (c) MEMS chip.

A conceptual DWDM is designed with two filter channels. Two sockets for inserting the filters are arranged symmetrically on a 1 cm x 1 cm chip with a 5 degree angle to the incident light. Another active lock is laid on the opposite edge of the chip for a micromirror, which is used to redirect the reflected light from one filter to another. The micromirror with the dimension of 675 μm (L) x 585 μm (w) x 100 μm (t) is fabricated by the similar process in section 4.3 with additional backside etching. Otherwise, etch holes have to be added which will introduce excessive transmission losses of the reflected optical energy and degrade the optical performance of the micromirror.

The assembly process of the micromirror is the same as the one in section 4.5. The assembly of the filter does not require rotation. Due to the size and shape of the filter, it can be easily flipped by tweezers and picked up by vacuum gripper. The assembled two filters and a micromirror are shown in Fig. 5.2 (b).

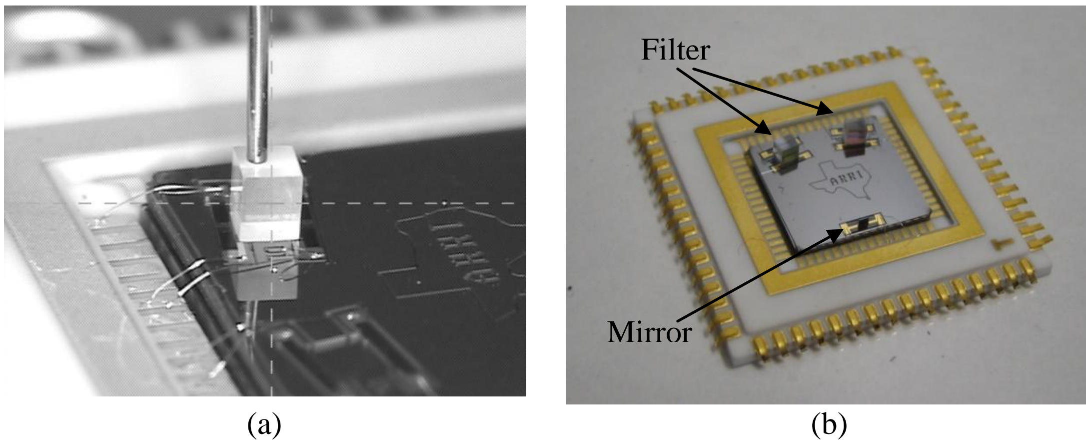

Figure 5.2 (a) A photo of inserting the filter into a socket with a vacuum gripper. (b) The assembled MEMS chip.

5.1.2. Experimental Demonstration

To characterize the optical performance of the assembled filter chips, the MEMS chip is mounted on the center of a rotation stage which is fixed on a 3-D transitional stage. The laser from the broadband source (1431 nm - 1631 nm) is coupled into a single-mode fiber connected to a Fiber Optic U-bench. The U-bench consists of fiber input and output with grin lens attached and aligned on the two arms. A 30 mm gap between the two arms allows MEMS chip to be placed in the optical path of the laser beam. The diameter of the optical beam coming out from the grin lens is less than 0.5 mm which is sufficient for passing through the filter chip whose size is more than 1 mm^2. The output fiber is connected to the optical spectrum analyzer (OSA).

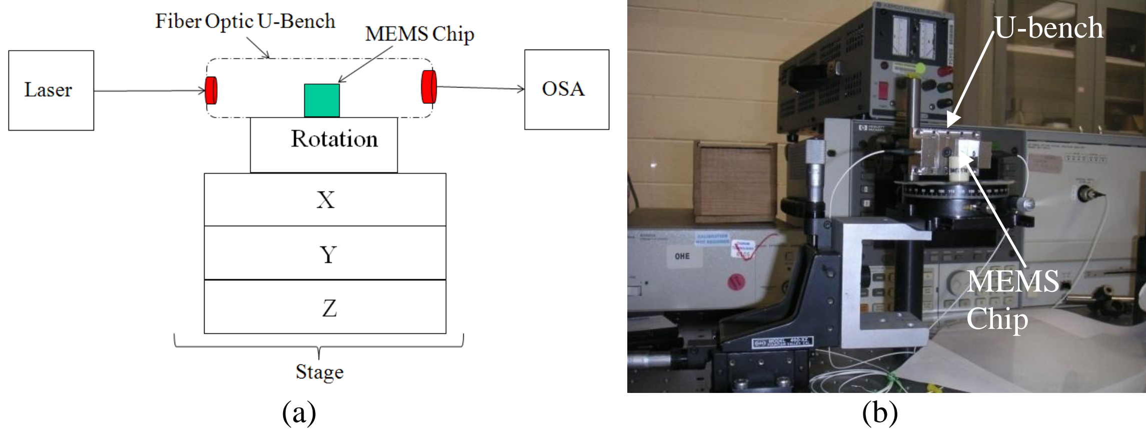

Figure 5.3 (a) The schematic drawing and (b) a photo of the optical measurement.

The holding force provided by the active lock is sufficient for the micromirror since both of them are in the same scale. However, the thickness of the filter is 12 times larger than the mirror. When flipping the assembled chip, the filters come off from the sockets because the gravitational force is much larger than the squeezing force of the

active lock. For the safety of the MEMS chip during transportation and optical measurement, super glue is applied on both the chevrons to freeze the actuators.

5.1.3. Results

Three experiments are performed to investigate the effect of assembly on the performance of the filters.

5.1.3.1. Direct Measurement of Filter Chips

The unassembled filter chips are measured directly by rotating the U-bench 90 ° and putting them on top of grin lens at one arm of the U-bench. Two chips of each channel are measured and the results are shown in Table 5.1.

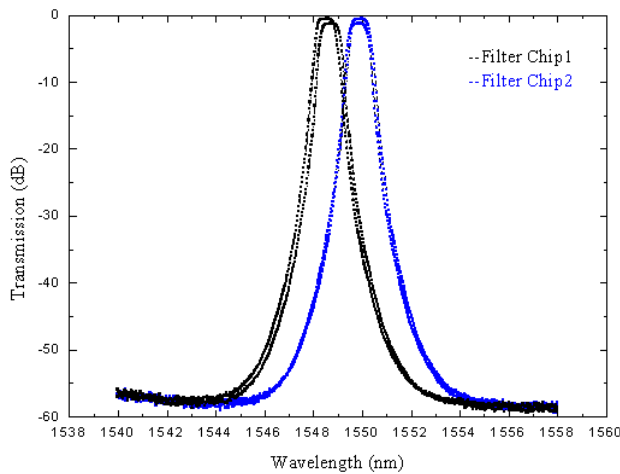

Figure 5.4 The plots of the transmission of the filters by direct measurement.

Table 5.1 The optical performance of the unassembled filter chips.

	Center Frequency (nm)	Transmission (dB)	3-dB Bandwidth (nm)	20-dB Bandwidth (nm)
Chip 1	1548.55	-0.54	0.85	1.725
	1548.68	-1.24	0.9	1.755
Chip 2	1549.95	-0.55	0.85	1.725
	1549.875	-1.24	0.9	1.725

5.1.3.2. Measured Results of the Assembled Chips

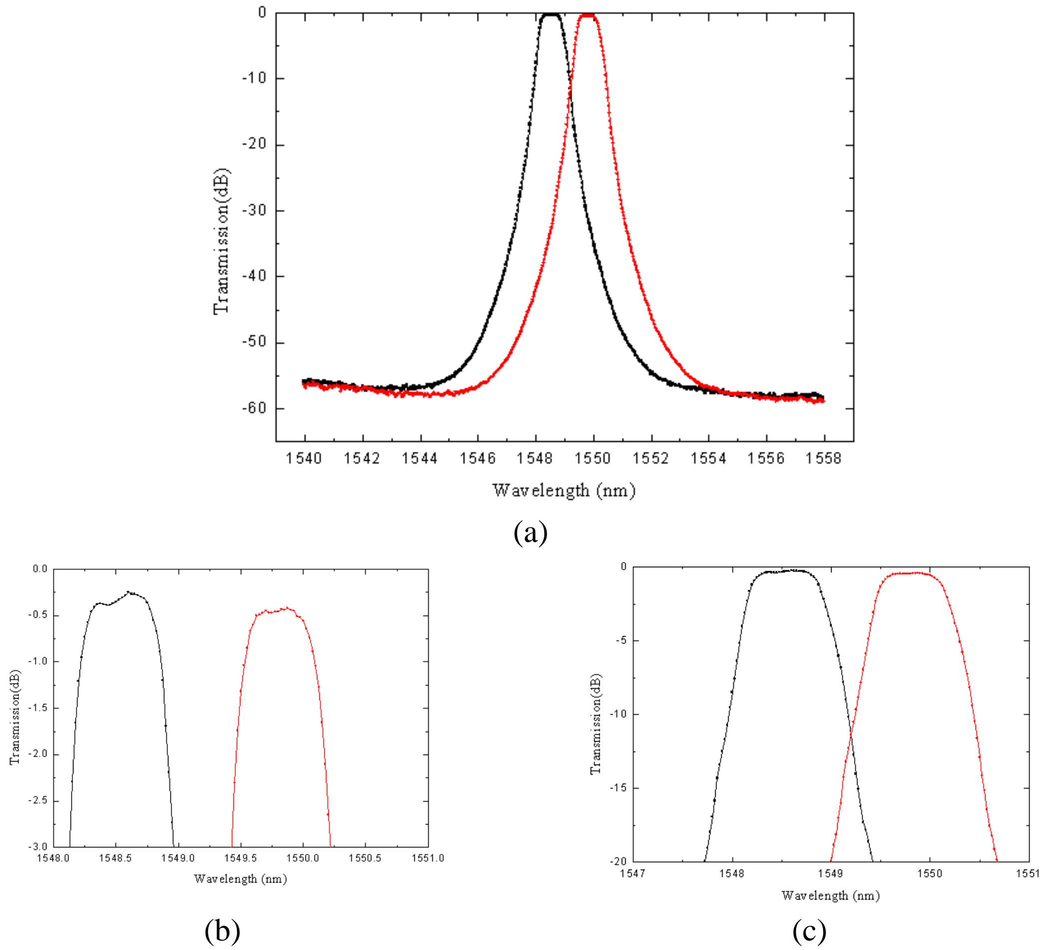

Figure 5.5 The measured (a) spectrum, (b) 3-dB bandwidths, and (c) 20-dB bandwidths of the assembled filters.

Table 5.2 The optical performance of the assembled filter chips.

	Center Frequency (nm)	Transmission (dB)	3-dB Bandwidth (nm)	20-dB Bandwidth (nm)
Filter 1	1548.60	-0.25	0.85	1.7
Filter 2	1549.65	-0.31	0.95	1.725

A further measurement is performed to investigate the relation between the angle of the incident light and the optical performance. In this experiment, the micromirror is taken out from the MEMS chip and one filter is aligned and fixed at the

center of the rotation stage. A series of measurement is taken by rotating the filter chip with a 1-degree-step resolution. Accordingly, only the angle of the incident light is changed in the experiment.

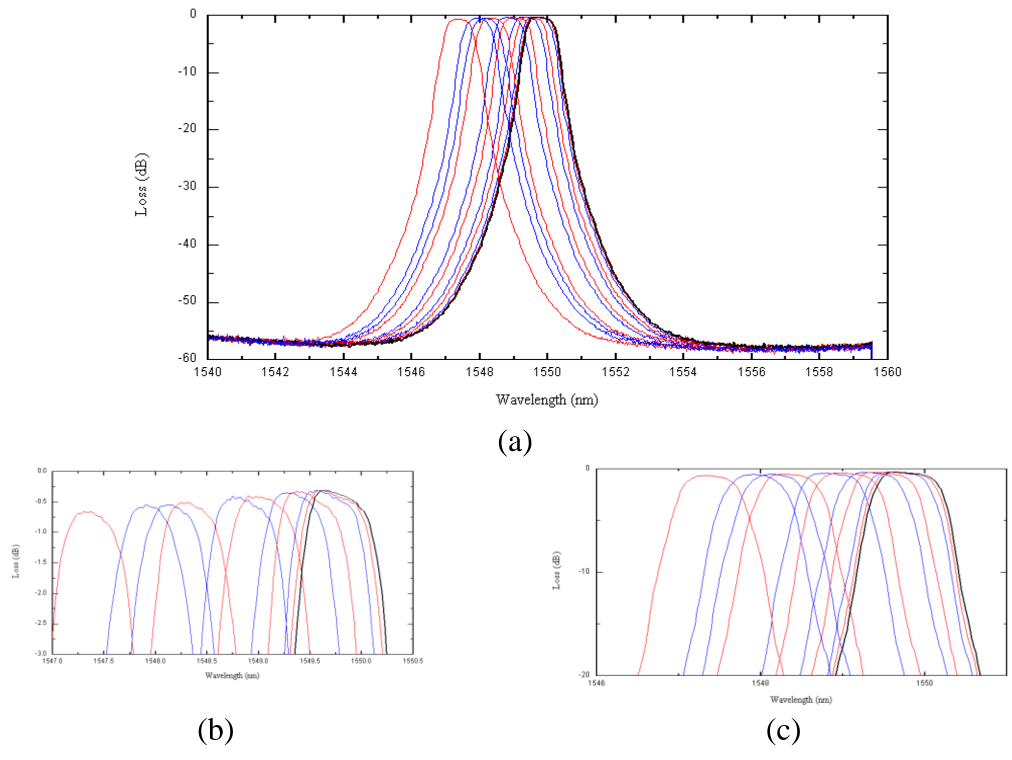

Figure 5.6 The measured (a) spectrum, (b) 3-dB bandwidths, and (c) 20-dB bandwidths of one assembled filter at 11 continuous angles.

Table 5.3 Optical performance at different angles.

Position	Center Frequency (nm)	Transmission (dB)	3-dB Bandwidth (nm)	20-dB Bandwidth (nm)
1	1547.95	-0.58	0.9	1.65
2	1548.125	-0.55	0.875	1.7
3	1548.75	-0.41	0.9	1.775
4	1549.275	-0.35	0.9	1.725
5	1549.575	-0.32	0.9	1.725
6	1549.65	-0.31	0.95	1.725
7	1549.6	-0.32	0.925	1.75
8	1549.375	-0.33	0.875	1.75
9	1548.975	-0.41	0.925	1.775
10	1548.3	-0.51	0.875	1.875
11	1547.325	-0.66	0.875	1.975

Table 5.4 Comparison of the optical performance.

	Company Data		Direct Measurement		Assembled Chip	
	Filter 1	Filter 2	Filter 1	Filter 2	Filter 1	Filter 2
Center Frequency (nm)	1548.9	1550.52	1548.55	1549.95	1548.60	1549.65
Transmission (dB)	-0.24	-0.24	-0.54	-0.55	-0.25	-0.31
3-dB Bandwidth (nm)	1.3	1.3	0.85	0.85	0.85	0.95

When compare the performance of measured data with the company data as shown in Table 5.4, the assembled DWDM filters demonstrated much lower insertion losses than the direct measurements. The insertion losses caused by assembly are 0.1 dB and 0.7 dB on the two filters. The discrepancy in the center frequency is believed causing by the angle of incident light. The sensitivity of the center frequency to the angle of incident light has demonstrated experimentally. It helps predict the optical performance of the filters at different angle. Accordingly, the optical path can be

planned on the MEMS chip and the active lock can be designed at the required destination with specific angles to achieve the ultimate performance of the system.

5.2 Active Parallel Assembly

Parallel assembly is considered to be a good manner for mass production in MEMS industry which is able to assemble multi-components simultaneously. Direct assembly is often considered as “serial assembly” due to the manipulations (grasp, rotate, joint, release) is sequential. Author believes that choosing the appropriate assembly technique should be depends on the application, because the configuration of the system decides the required manipulations and the assembly process. Parallel assembly is good at dealing a number of parts at the same time as discussed in section 1.3. Flip-chip bonding forms assembled parts with same heights while binding sites attracts thousands of identical parts and sorts of them through potential-energy well. Direct assembly can be used to construct complicated structures with high-aspect ratio to the substrate. The throughput of direct assembly is limited by the number of manipulators. If more than one manipulator can be arranged in 1-D or 2-D arrays, multi-components can be assembled simultaneously as well.

Using a row of twelve assembled micro jammers on one substrate to duplicate themselves has been investigated by assembling same amount jammers into snap sockets on another MEMS chip at Center for Automation Technologies, Rensselaer Polytechnic Institute. The cumulated alignment error increased the difficulty for the assembled jammer to pick up the microparts. The snap fasteners utilized could not provide sufficient stiffness for the assembled jammer to insert microparts into sockets.

Epoxy was used to enhance the stiffness of the snap lock by dipping the jammer into it before assembly. However, the curing stress introduced significant alignment tolerance. The experiment demonstrates the successful assembly using "assembled assembler" largely depends on: (1) sufficient stiffness provided by the sockets to the assembled manipulators to perform assembly task, and (2) a larger tolerance provided by the sockets into which the microparts will be inserted to compensate the alignment error.

The active locking mechanism fulfills both of the two requirements mentioned above and possesses the potentials of enabling the "active parallel assembly". First, by carefully choosing and designing the actuators, the active lock can provide 40 μm or even larger compensation for inserting microparts. Second, zero insertion force is required during assembly since there is no direct interaction between the sockets and the micropart. Third, a permanent manner of the assembled part can be achieved by soldering or applying epoxy. When the assembled part is fixed and served as the manipulator to assemble other parts into active locks, it's only required to provide a force that can grasp and release the part which can be implemented by stiction or other types of forces. The assembled manipulator possesses the ability of inserting microparts into the demonstrated snap-fasteners and clamp lock that fabricated by SOI wafer according to the force requirement as shown in Table 5.4. The stiffness of the sockets can be improved by a good quality of soldering.

Table 5.5 Force characterizations demonstrated experimentally.

		Tolerance (μm)	Complete Insertion Force (mN)	Pull Out Force (mN)
Snap Fastener			18	<18mN
Clamp Lock [1.27]			3	>12
Active Lock	DCM	44	0	3
	SCM	12	0	19 (without) and 39.9 (with soldering)

The micropart served as the manipulator can be either passive (no actuation required) or active (need actuation). One assembled electrothermal microgripper [5.2] using the active lock is shown in Fig. 5.7 (a). More than one microgrippers can be assembled in the same way to form a 2-D array to perform assembly task as illustrated in Fig. 5.7 (b). The maximum number of manipulators is limited by the precision of alignment and tolerance provided by the sockets. The orthogripper [1.27] with the ability of rotating assembled parts can also be utilized to avoid the rotation on the manipulator.

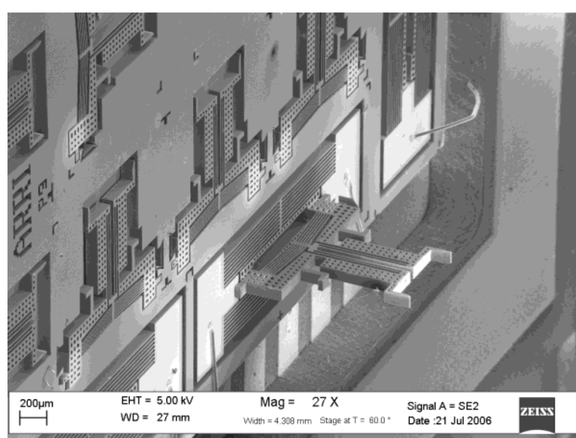

(a)

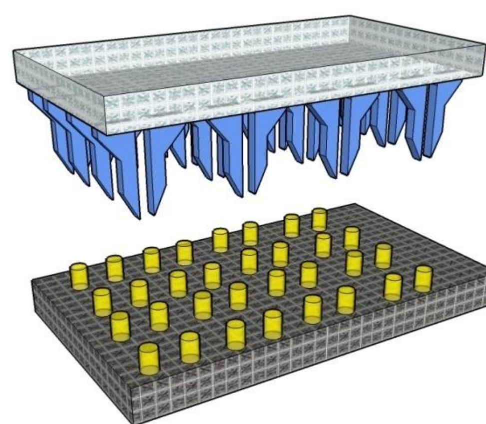

(b)

Figure 5.7 (a) An SEM photo of one assembled microgripper using active joining mechanism. (b) A schematic drawing of an array of assembled microgrippers manipulating microparts.

For the assembled active microgrippers, electrical signal is required to excite the actuation. Electrical path can be formed through the inserted finger and sockets. Solder bonding can be opted to form the electrical interconnection as discussed in section 4.6.

5.3 Future Work

The integration of micro systems includes three major tasks. First, assemble individual devices into a common MEMS platform. Second, combine the MEMS platform with conventional IC which can provide control and power signal. Third, cap the integrated system into a vacuum and hermetic package to be protected from contamination. Currently the MEMS integration and packaging is the most expensive part in micromachining. The cost is up to and exceeding 75% of the total cost. The key issues are free standing structures, hermetic sealing and temperature sensitive microelectronics [5.3].

The assembly platform using active joining mechanism demonstrates a good feasibility for free standing microstructures. It’s compatible in the dimensions with the commercially available components, which allow each of them to be fabricated under its optimized conditions. The precisely robotic manipulations dramatically reduce the time of assembly and provide alignment accuracy in micron scale, which allows individual components to achieve their best performance. The synthesis of the best performed devices optimizes the functions as well as reduces the size and weight of the integrated system.

Fluxless soldering can be applied to the interface to form bonding and electrical interconnects for the assembled microstructures. The electrical path from the substrate

to the vertical interconnects can enable the out-of-plane motions on the assembled devices, which will dramatically increase the applications in many fileds, such as RF (Radio Frequency) devices and free space optical systems. The challenges will be how to minimize the interface loss and the power consumption. The solder bonding procedure can be performed simultaneously with the hermetic sealing of the MEMS chip through reflow process if the same solder material is used for both purposes. Otherwise they can be done separately according to the melting point of different solder metals.

Figure 5.8 illustrates the architecture of a miniature micro interferometer. The components, including a laser diode, a detector, a lens, a beam splitter, two micro mirrors, will all be interconnected by the active locks on the substrate. The lens, laser diode, detector and beam splitter can all be opted from commercial products to provide good optical performance. The sockets can be designed according to the geometry of each component to facilitate the assembly. The moving mirror can be attached to the actuators that made on the substrate by solder bonding or epoxy. The actuator can also be made by other materials that offer larger deflection, such as polysilicon and piezo material, and attached to the substrate by solder materials. With the MEMS enhanced micro interferometer, the size, weight and power consumption will be dramatically reduced. It enables the miniature system to work in different environments compared with the limited utility of the current bulky and heavy system.

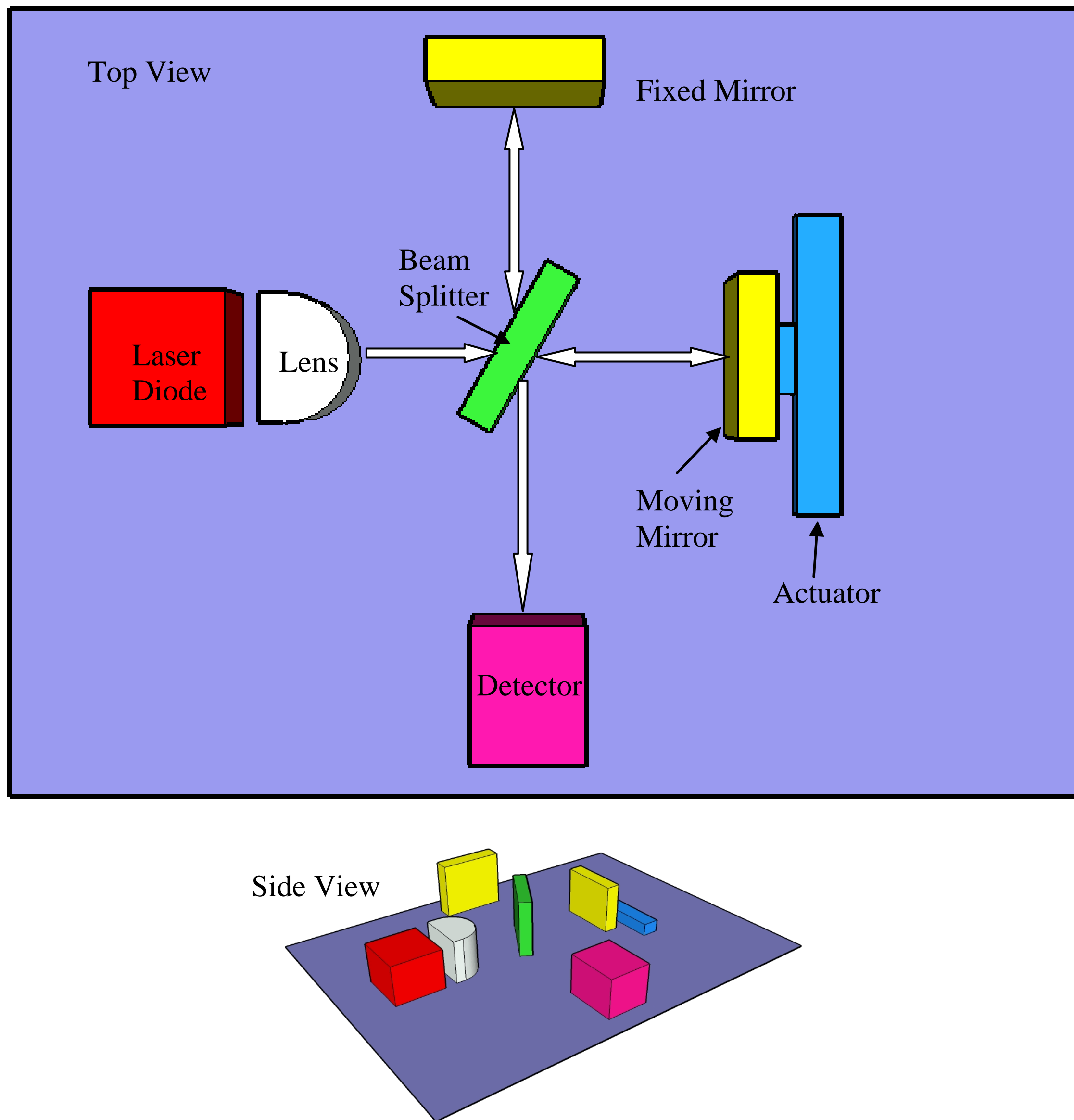

Figure 5.8 The schematic drawing of a miniature micro spectrometer.

Multi-level stacking has been demonstrated by wafer and chip boning. Multi-link microstructures can be constructed using the same active joining strategy which can enable more complex devices such as micro robots with several degrees of freedom (DOF). The 3-D assembly stations in macro world can manipulate microparts by using the end-effecters (microgrippers) which are made in the same scale as the manipulated

parts. The assembled micro robots may be combined with the end-effecters in nanometer scale to assemble nanoparticles and molecules in the future. These micro or nano robots may also be integrated with wireless modules for biology and medical applications, such as performing robotic surgery in the body of a human being.

The assembled MEMS structures can be further integrated with IC chips and then packaged. The integrated system offers many advantages, such as small size, light weight, and more functions. They are portable and less expensive. They can be used in 3-D display, unmanned vehicle for sensing and preventing collision, and implanted chip to monitor the health conditions, even in our brain to record our memories.

The helmet is assembled in the stadium of Dallas Cowboys using active joining mechanism is shown in Fig. The purpose is to demonstrate the assembly of complex microstructures. It's also a fond memory of my work in Dallas.

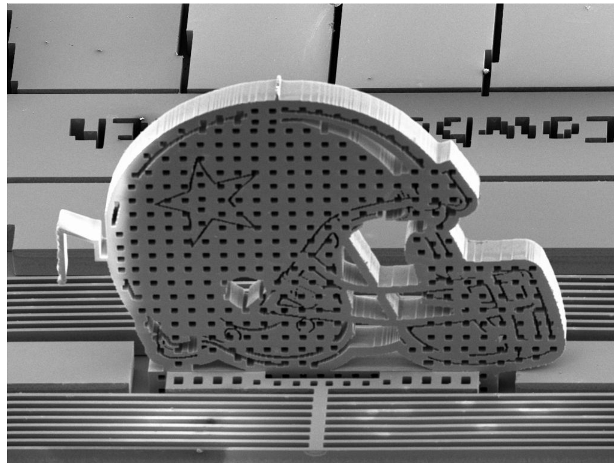

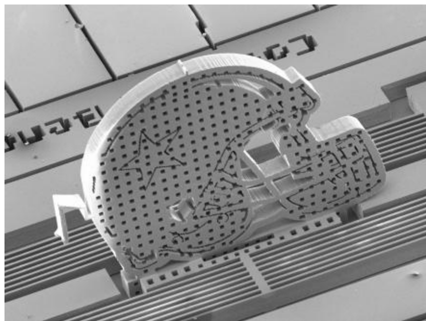

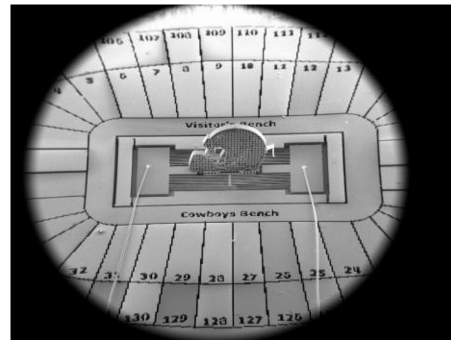

Figure 5.9 The SEM photos of an assembled micro helmet in the stadium of Dallas Cowboys.

CHAPTER 6

CONCLUSION

In this dissertation, two approaches of integrating 3-D MEMS components have been investigated. First, a polymer based Fabry-Perot filter is designed, fabricated and characterized. The highly mechanical integrity and low optical loss is successfully demonstrated.

Second, a new active joining mechanism is demonstrated by two designs. Chevron actuators are used as part of the sockets to open and squeeze the inserted microparts. The active locks and microparts are fabricated on a SOI wafer then characterized. Microgrippers, jammers and multi-layer thin-film filters are constructed by the active locks with a 100% successful rate using direct assembly. The benefits of this joining method lie in: (a) avoid the insertion force; (b) the destination of the microparts to be assembled can be predefined on the chip and the assembled devices are precisely self-aligned; (c) misalignment or damaged devices can be corrected and replaced by opening the active lock and redo assembly; (d) the shape of the sockets can be arbitrary according to the geometry of the devices to be assembled; (e) decoupling the fabrication process of the assembled devices and the platform (substrate) of assembly. It allows all the components to be fabricated under their optimized conditions then combine the advantages of different technologies. Fluxless soldering can also be

applied on the active lock to form electrical path and enhance the stiffness of the mechanical connection.

Therefore, it can significantly reduce the size, weight, and cost through the integrated systems. This new technique will have impacts and applications in free-space optical systems, complex micro robots, and packaging of 3-D MEMS components.

REFERENCES

[1.1] M. M. Maharbiz, M. B. Cohn, R. T. Howe, R. Horowitz, and A. P. Pisano, "Batch Micropackaging by Compression-Bonded Wafer-Wafer Transfer," *MEMS '99,* Orlando, FL, January 17-21, 1999, pp. 482-9.

[1.2] M.M. Maharbiz, R.T. Howe, and K.S.J. Pister, "Batch transfer assembly of microcomponents onto surface and SO1 MEMS," presented at *Transducers '99 Conference*, Sendai, Japan, June 7-10, 1999.

[1.3] A. Singh, D. Horsely, M. Cohn, A. Pisano, and R. Howe, "Batch transfer of microstructures using flip-chip solder bonding," *IEEE Journal of Microelectromechanical Systems*, Vol. 8, No. 1, pp. 27-33, March, 1999.

[1.4] W. Piyawattanametha, P. R. Patterson, D. Hah, H. Toshiyoshi, and M. C. Wu, "A 2D Scanner by Surface and Bulk Micromachined Angular Vertical Comb Actuators," *IEEE/LEOS Int. Conf. on Optical MEMS and Their Applications (MOEMS '03)*, Outrigger Waikoloa Beach, Hawaii, USA, Aug. 18 - 21, 2003.

[1.5] K. Fu, A.J. Knobloch, F.C. Martinez, D.C. Walther, A.C. Fernandez-Pello, A.P. Pisano, and D. Liepmann, "Design & Fabrication of a Silicon-Based MEMS Rotary Engine," *IMECE/MEMS-23925, Proc. ASME 2001 Int'l Mech. Engin. Congress & Expo. (IMECE),* New York, November 2001.

[1.6] A. V. Krishnamoorthy, A. L. Lentine, K. W. Goossen, J. A. Walker, T. K. Woodward, J. E. Ford, G. F. Aplin, L. A. D'Asaro, S. P. Hui, B. Tseng, R. E. Leibenguth, D. Kossives, D. Dahringer, L. M. F. Chirovsky, and D. A. B. Miller, "3-D integration of MQW modulators over active submicron CMOS circuits: 375 Mb/s transimpedance receiver-transmitter circuit," *IEEE Photon. Technol. Lett.*, Vol. 7, No. 11, pp. 1288–1290, 1995.

[1.7] M. Cohn, C. J. Kim, A.P. Pisano, "Self-Assembling Electrical Networks: An Application of Micromachining Technology," *Proceedings of the Int. Conf. on Solid State Sensors and Actuators*, San Francisco, CA, Jun. 24-27, 1991, pp. 490-493.

[1.8] K. F. Böhringer, K. Goldberg, M. B. Cohn, R.T. Howe, and A. P. Pisano, "Parallel Microassembly with Electrostatic Force Fields," *Proc. IEEE Conf. on Robotics and Automation*, Leuven, Belgium, May 1998, pp. 1204-11.

[1.9] U. Srinivasan, M.A. Helmbrecht, C. Rembe, R. S. Muller, and R.T. Howe, "Fluidic Self-Assembly of Micromirrors onto Microactuators Using Capillary Forces," *Journal of Selected Topics in Quantum Electronics*, Jan. 2002.

[1.10] U. Srinivasan, M. A. Helmbrecht, R. S. Muller and R. T. Howe, "MEMS: Some Self Assembly Required," *Optics & Photonics News*, Vol. 13, No. 11, pp. 20-24, Nov. 2002.

[1.11] S.R. Burgett, K.S.J. Pister, and R.S. Fearing, "Three Dimensional Structures Made With Microfabricated Hinges," in *MicroMechanical Systems, ASME Winter Annual Meeting*, Vol. 40, Anaheim, pp. 1-11, CA, 1992.

[1.12] T. Ebefors, J. Ulfstedt-Mattsson, E. Kälvesten, and G. Stemme, "3D micromachined devices based on Polyimide Joint technology," *SPIE Symposium on Microelectronics and MEMS*, Vol. 3892, pp. 118-132, Gold Coast, Queensland, Australia, October, 1999.

[1.13] K.F. Harsh, V.M. Bright, and Y.C. Lee, "Solder Self-Assembly for Three-Dimensional Microelectromechanical Systems," *Sensors and Actuators A*, Vol. 77, pp. 237-244, 1999.

[1.14] L.Y. Lin, E. Goldstein and R.W. Tkach, "Free-space micromachined optical switches with sub-millisecond switching time for large scale optical cross connect," *IEEE Photo. Tech. Lett.* Vol. 10, pp. 525-527, 1998

[1.15] L.Y. Lin, E. Goldstein and R.W. Tkach, "Free-space micromachined optical switches for optical networking," *Selected Topics in Quantum Electronics, IEEE Journal,* Vol. 5, Issue 1, pp. 4-9, 1999.

[1.16] O. Solgaard, M. Daneman, N. C. Tien, A. Friedberger, R. S. Muller, and K. Y. Lau, "Optoelectronic packaging using silicon surface micromachined alignment mirrors," *IEEE Photon. Technol. Lett.*, Vol. 7, pp. 41–43, Jan. 1995.

[1.17] S. S. Lee, L. Y. Lin, and M. C. Wu, "Surface-micromachined free-space micro-optical systems containing three-dimensional micro-gratings," *Appl. Phys. Lett.,* Vol. 67 , No. 15, pp. 2135-2137, 1995.

[1.18] L. Y. Lin, J. L. Shen, S. S. Lee, and M. C. Wu, "Surface-micromachined micro-XYZ stages for free-space micro-optical bench," *IEEE/LEOS 1996 Summer Topical*

Meetings on Optical MEMS and Their Applications, Keystone Resort, COY Aug. 5-9, 1996.

[1.19] J. Zou, C. Byrne, C. Liu, and D. Brady, "Optical properties of surface micromachined mirrors with etching holes," *Journal of Microelectromechanical Systems,* 8(4): pp. 506-513, 1999.

[1.20] *Handbook of Semiconductor Silicon Technology*, Ed. by W.C. O'Mara, R.B. Herring, and L.P. Hunt, 1990.

[1.21] R.S. Fearing, "Survey of Sticking effects for Micro-parts," in *IEEE Int. Conf. Robotics and Intelligent Systems IROS '95*, 1995, Pittsburgh, PA.

[1.22] Zyvex Inc. www.zyvex.com

[1.23] K. Tsui, et al, "Micromachined end-effector and techniques for directed MEMS assembly," *Journal of Micromechanics and Microengineering*, 2004, Vol. 14, pp. 542-549.

[1.24] G. Skidmore, et al, "Assembly technology across multiple length scales from the micro-scale to the nano-scale.," in *17th International Conference on MEMS*, 2004.

[1.25] N. Dechev, W.L. Cleghorn, and J.K. Mills, "Microassembly of 3-D MEMS Structures Utilizing a MEMS Microgripper with a Robotic Manipulator," In *International Conference on Robotics &Automation*, 2003,Taipei, Tsiusn.

[1.26] N. Dechev, W.L. Cleghorn, and J.K. Mills, "Microassembly of 3-D microstructures using a compliant, passive microgripper," *Journal of Microelectromechanical Systems*, 2004. Vol. 13(2), pp. 176-189.

[1.27] M. Last, V. Subramaniam, and K. S. J. Pister, "Out of Plane Motion of Assembled Microstructures using a Single-Mask SOI Process," *Proc. 13th International Conference on Solid-State Sensors, Actuators and Microsystems*, IEEE, New-York, June 2005.

[1.28] H. Han, L. Weiss and M.L. Reed, "Micromechanical Velcro," *Journal of Microelectromechanical Systems*, Vol. 1, pp. 37–43, 1992.

[1.29] H. Han, L. Weiss, and M.L. Reed, "Mating and piercing micromechanical structures for surface bonding applications," *Proceedings of the 1991 Micro Electro Mechanical Systems (MEMS '91), An Investigation of Micro Structures, Sensors, Actuators, Machines and Robots*, February, 1991, pp. 253 - 258.

[1.30] R. Prasad, K.-F. Bohringer, and N. C. MacDonald. "Design, fabrication, and characterization of SCS latching snap fasteners for micro assembly," in *Proceedings of the ASME International Mechanical Engineering Congress and Exposition (IMECE)*, San Francisco, California, Nov. 1995.

[1.31] V. Subramaniam, *Serial Assembly of Microstructures*, University of California, Berkeley, May 2006.

[2.1] C.R. King, L.Y. Lin, and M.C. Wu, "Monolithically integrated refractive microlens standing perpendicular to the substrate," *Proc. SPIE,* Vol. 2687, pp. 123-130, 1996.

[2.2] L.Y. Lin, S.S. Lee, K.S.J. Pister, and M.C. Wu, "Three-dimensional micro-Fresnel optical elements fabricated by micromachining technique," *Electron Lett*, Vol. 30, No. 5, pp. 448-49, 1994.

[2.3] *PolyMUMPs Design Handbook. Rev. 11.0*, MEMSCap Inc.

[2.4] T. Akiyama and K. Shono, “Controlled stepwise motion in polysilicon microstructures,” *J. Microelectromech. Syst.*, Vol. 2, No. 3, pp. 106–110, Sept. 1993.

[2.5] T. Akiyama and H. Fujita, “A quantitative analysis of scratch drive actuator using buckling motion,” in *Proc. IEEE Microelectromech. Syst.*, Amsterdam, The Netherlands, Feb. 1995, pp. 310–315.

[2.6] K.S.J. Pister, M.W. Judy, S.R. Burgett, and R.S. Fearing, “Microfabricated hinges,” *Sensors and Actuators A (Physical),* Vol. A33, No. 3, June 1992, pp. 249-56.

[2.7] M.C. Wu, L.Y. Lin, S.S. Lee and K. Pister, “Micromachined free-space integrated micro-optics,” *Sensors and Actuators A*, Vol. 50, pp. 127, 1995.

[2.8] J-.C. Chiao, Y. Fu, D. Choudhury and L.-Y. Lin, “MEMS millimeterwave components,” *The IEEE-MTT-S International Microwave Symposium*, Anaheim, CA, June 13-19, 1999.

[2.9] *Handbook of optical constants of solids*, Academic Press Inc. ISBN 0-12-544420-6, pp. 547-569, 1985.

[2.10] www.hdmicrosystems.com

[2.11] J. Zou, C. Byrne, C. Liu, and D. Brady, “Optical properties of surface micromachined mirrors with etching holes,” *Journal of Microelectromechanical Systems,* Vol. 8, No.4, pp. 506-513, 1999.

[2.12] *Technical information of PI2730 series process*, HD Microsystems Inc.

[2.13] H. Lorenz, M. Laudon, and P. Renaud, “Mechanical characterization of a new high-aspect-ratio near UV-photoresist,” *Microelectron. Eng.*, Vol. 41–42, pp. 371–374, Mar. 1998.

[2.14] *Technical information of CYCLOTENE™ 4000 Series Advanced Electronic Resins (Photo BCB)*, The Dow Chemical Company.

[2.15] *Technical information of PI2610 series process*, HD Microsystems Inc.

[3.1] M. Mayyas, P. Zhang, W.H. Lee, P. Shiakolas, and D. Popa, “Design Tradeoffs for Electrothermal Microgrippes,” in *IEEE International Conference on Robotics and Automation*, Apr. 10-14 2007, Rome, Italy.

[3.2] A.N. Das, P. Zhang, W.H. Lee, D. Popa, and H. Stephanou, “μ^3: Multiscale, Deterministic Micro-Nano Assembly System for Construction of On-Wafer Microrobots,” in *2007 IEEE International Conference on Robotics and Automation*, Apr. 10-14, 2007, Rome, Italy.

[4.1] W.C. Tang, T.C.H. Nguyen, and R.T. Howe, “Laterally driven polysilicon resonant microstructures,” *Sensors and Actuators*, Vol. 20, pp. 25-32, 1989.

[4.2] Q.-A. Huang and N. K. S. Lee, “Analysis and design of polysilicon thermal flexure actuator,” *J. Micromech Microeng*, Vol. 9, pp. 64–70, 1999.

[4.3] J.H. Comtois, and V.M. Bright, “Surface micromachined polysilicon thermal actuator arrays and applications,” in *Proc., Solid-state Sensor and Actuator Workshop*, pp. 174-177, June 1996.

[4.4] J.H. Comtois, M.A. Michalicek, and C.C. Barron, “Characterization of electrothermal actuators in a four level planarized surface-micromachined

polycrystalline process," in *Proc., IEEE Intl. Conf. on Solid-state Sensors,* Vol. 2, pp. 769-772, 1997.

[4.5] W**.** YE, S. Mukherjee, and N. MacDonald, "Optimal shape design of an electrostatic comb drive in MEMS," *J. of Microelectromech. Syst.*, Vol 7**,** pp. 16–26, 1998.

[4.6] L. Que, J.-S. Park, and Y.B. Gianchandani, "Bent-beam electro-thermal actuators for high force applications," *IEEE International Conference on Microelectromechanical systems (MEMS)*, pp. 31–36, 1999.

[4.7] M.J. Sinclair, "A high force low area MEMS thermal actuator," in *ITHERM 2000: Proc. 7th Intersociety Conf. on Thermal and Thermomechanical Phenomena,* Las Vegas, NV, May 23–26, 2000, pp 127–32.

[4.8] J.-S. Park, L. L. Chu, E. Siwapornsathain, A. D. Oliver, and Y. Gianchandani, "Long throw and rotary output electro-thermal actuators based on bent-beam suspensions," in *Proc. IEEE International Conference on Micro Electro Mechanical Systems (MEMS00)*, Miyazaki, Japan, Jan. 2000, pp. 680–685.

[4.9] *Technical Note: The AE-800 Series Sensor Elements*, Sensor One Technology Corp.

[4.10] *Gold Tin – The unique eutectic solder alloy*, Indium Corporation of America.

[4.11] J. Kim, and C.C. Lee, "Fluxless wafer bonding with Sn-rich Sn-Au duallayer structure, " *Materials Science and Engineering A*, Vol. 417, No. 1-2, Feb 15, 2006, pp. 143-148.

[4.12] J. Kim, and C.C. Lee, “Fluxless flip-chip Sn-Au solder interconnect on thin Si wafers and Cu laminated polyimide films,” *Materials Science and Engineering A*, Vol. 416, No. 1-2, Jan 25, 2006, pp. 74-79.

[4.13] T. Nishikawa, M. Ijuin, and R. Satoh, “Fluxless soldering process technology,” *Proceedings of Electronic Components and Technology Conference*, 1994, pp. 286-292.

[4.14] N. Koopman, S. Bobbio, S. Nangalia, J. Bousaba, and B. Piekarski, “Fluxless soldering in air and nitrogen”, *Proceedings of Electronic Components and Technology Conference*, 1993, pp. 595-605.

[5.1] Barr Associates, Inc. www.barrassociates.com

[5.2] M.A. Mayyas, W.H. Lee, D.O. Popa, P. Shiakolas, P. Zhang, and H. E. Stephanou, “Comprehensive Electrothermal Modeling of a Thermal Microgripper,” *TEXMEMS VII International Conference on MEMS*, El Paso, TX, September 2005.

[5.3] L.W. Lin, *Packaging Schemes for MEMS*, University of California at Berkeley, Jun. 2004.

BIOGRAPHICAL INFORMATION

Ping Zhang received her B.S. in the Department of Electrical Engineering at the Tianjin University in 2000 and M.S. degree in the Department of Physics at the University of Massachusetts Dartmouth in 2002, respectively. She joined MEMS group at UTA since 2002 and then became a research assistant at the Automation and Robotic Research Institute since May 2005. She received her Ph.D. degree in the Electrical Engineering Department at the University of Texas Arlington in May 2007. In her Ph.D study, she has authored and coauthored more than 10 technical papers. Her areas of expertise include MEMS design, fabrication, 3-D microassembly, packaging, free space optics, WDM devices and thin film filters.